Earth and Planetary Science Letters 396 (2014) 235–251

Contents lists available at ScienceDirect

Earth and Planetary Science Letters

www.elsevier.com/locate/epsl

Burial and exhumation during Archean sagduction in the East Pilbara Granite-Greenstone Terrane

C. François [a,b,*], P. Philippot [a], P. Rey [b], D. Rubatto [c]

[a] Equipe Géobiosphère Actuelle et Primitive, Institut Physique du Globe de Paris-Sorbonne Paris Cité, Paris Diderot UMR 7154 CNRS, 1 rue Jussieu, F-75005 Paris, France
[b] EarthByte Research Group, School of Geosciences, University of Sydney, NSW 2006, Sydney, Australia
[c] Research School of Earth Sciences, The Australian National University, Canberra 0200, Australia

ARTICLE INFO

Article history:
Received 15 January 2014
Received in revised form 8 April 2014
Accepted 10 April 2014
Available online 3 May 2014
Editor: T.M. Harrison

Keywords:
Archean tectonics
sagduction
thermobarometry
geochronology
numerical simulation

ABSTRACT

Archean granitic domes and intervening volcano-sedimentary basins are commonly interpreted as the product of "sagduction", a process involving the gravitational sinking of surficial greenstone cover sequences into narrow belts and the coeval exhumation of deeper granitic crust into broad domes. Alternatives to the sagduction model that can account for the regional dome and basin pattern include fold interferences and extensional metamorphic core complexes. In order to provide quantitative constraints on the pressure–temperature–time (P–T–t) evolution experienced by greenstone–granite pairs we investigate the Warrawoona greenstone belt and adjacent Mount Edgar granitoid dome the East Pilbara craton (Western Australia). We adopt a multidisciplinary approach that includes structural, metamorphic, geochronological and numerical investigation of the 3.5–3.2 Ga Mount Edgar high-grade metamorphic rocks. Garnet-bearing metasediments and metabasalts collected along the SW and SE rims of the Mount Edgar Dome show higher pressure but lower temperature of equilibration (9–11 kbar and 450–550 °C) than enclaves collected in the core of the dome (6–7 kbar and 650–750 °C). In situ oxygen isotope analysis and U–Pb dating of zircons from the enclave indicate a metasedimentary origin ($\partial^{18}O \sim +13‰$) for the protoliths and a metamorphic age of 3311.9 ± 4.9 Ma. In addition, monazites included in garnet from the SW dome margin yield an age of 3443.4 ± 4.5 Ma. These monazites suggest the existence of an older metamorphic cycle and imply a polymetamorphic evolution of the unit. The P–T–t data support fast, gravity-driven tectonics, wherein sedimentary rocks were buried to lower crustal conditions, metamorphosed and exhumed back to the surface during a cycle lasting only a few million years. Forward thermo-mechanical modeling confirms the P–T–t evolutions deduced from thermobarometry and geochronology. Our model shows a large range of possible apparent geothermal gradients during sagduction, including low apparent geothermal gradients that are similar to those proposed for Archean and modern subduction.

1. Introduction

Archean continents have many attributes that set them apart from post-Archean counterparts. The relative abundance of komatiites in the Archean reflects hotter mantle than today (Arndt and Nisbet, 1982; Hoffman, 1988; Abbott et al., 1994; Jaupart et al., 2007; Coltice et al., 2009) and possibly widespread mantle plume activity (Condie and Benn, 2006). One of the most striking characteristics of Archean terranes is the systematic presence of thick, denser, continental flood basalts (greenstone covers) on felsic and therefore less dense crusts (Abbott and Hoffman, 1984; Taylor and McLennan, 1985; Bickle, 1986; Hoffman and Ranalli, 1988; Smithies et al., 2003). The combination of density inversion and hotter Archean crustal geotherm due to higher U–Th–K content conspired to make this stratigraphy mechanically unstable (e.g. Macgregor, 1951; Ramberg, 1967; Anhaeusser, 1973; Mareschal and West, 1980; Dixon and Summers, 1983; Chardon et al., 1996; Chardon et al., 1998; Collins et al., 1998). The coupled foundering of greenstone covers into narrow basins and exhumation of the deeper felsic crust into granitic domes has been named sagduction (Macgregor, 1951) and is, at least in part, responsible for the dome-and-basin pattern in many Archean cratons. This process corresponds to a partial convective overturn (Collins et al., 1998;

* Corresponding author at: Equipe Géobiosphère Actuelle et Primitive, Institut Physique du Globe de Paris-Sorbonne Paris Cité, Paris Diderot UMR 7154 CNRS, 1 rue Jussieu, F-75005 Paris, France. Tel.: +33 183957727.
E-mail address: francois@ipgp.fr (C. François).

http://dx.doi.org/10.1016/j.epsl.2014.04.025
0012-821X/

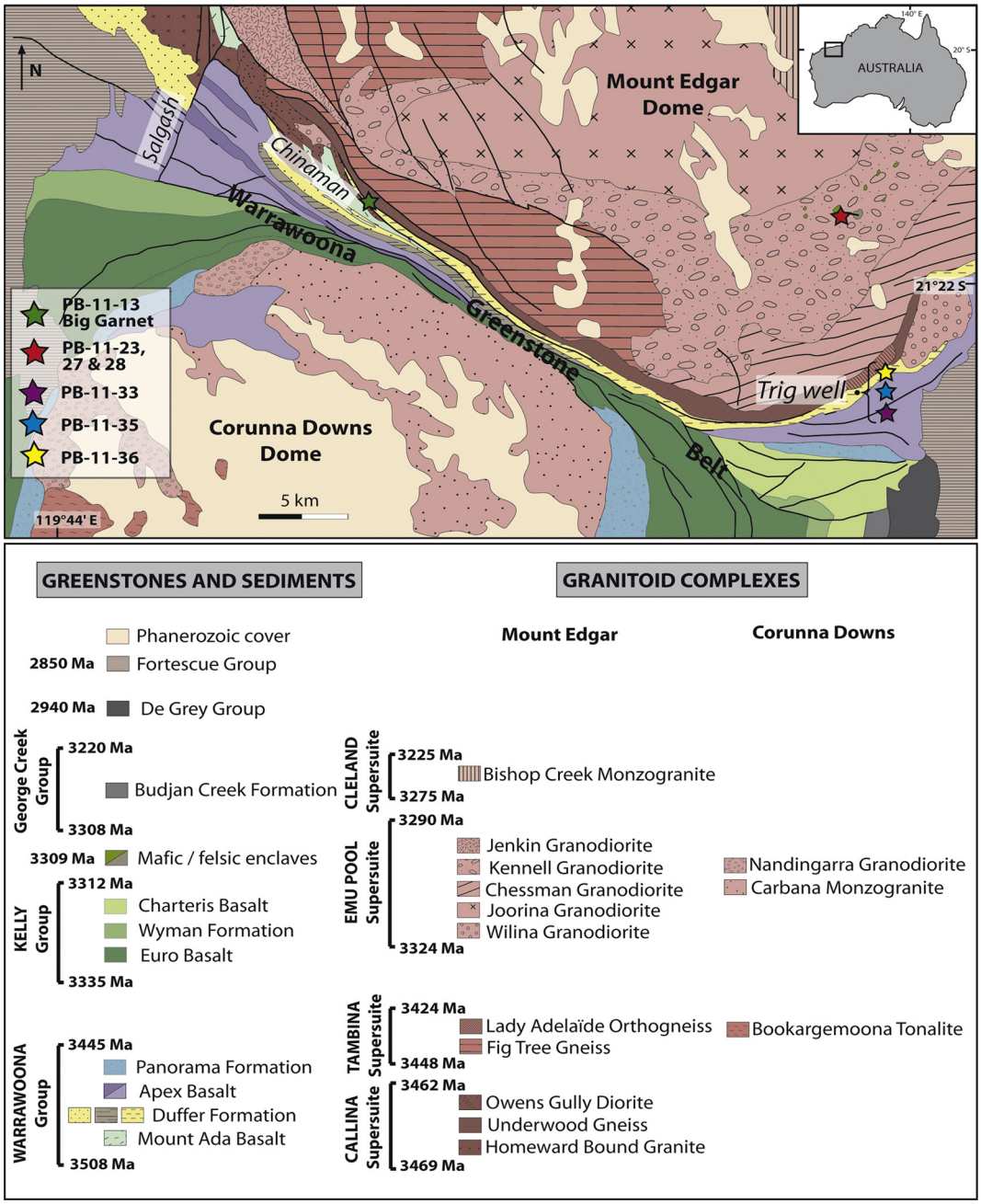

Fig. 1. Geological map of the southern part of Mount Edgar granitoid, the Warrawoona Greenstone Belt and the northern part of Corunna Downs granitoid. See location in Fig. S1 in supplementary data. Colored stars show sample locations. Age data from Williams and Collins (1990), Thorpe et al. (1992), McNaughton et al. (1993), Buick et al. (1995), Barley and Pickard (1999), and Nelson (1999, 2001a). Map after Williams and Bagas (2007), Mount Edgar, WA Sheet 2955: Geological Survey of Western Australia, 1:100 000 Geological Series and Hickman and Van Kranendonk (2008), Marble Bar, WA Sheet 2855: Geological Survey of Western Australia, 1:100 000 Geological Series. (For interpretation of the references to color in this figure, the reader is referred to the web version of this article.)

Van Kranendonk et al., 2004), which tends to create the density inversion and promote the cooling of the geotherm via the concentration of U–Th–K in the upper part of the crust (West and Mareschal, 1979). In the Archean, sagduction was a process able to drive crustal scale deformation, involving deep burial and exhumation, far away from plate margins where plate tectonic processes tend to focus. Sagduction has been the focus of structural studies (e.g. Bouhallier et al., 1993; Percival et al., 1994; Bouhallier et al., 1995; Chardon et al., 1996; Chardon et al., 1998; Collins et al., 1998; Bédard et al., 2003; Peschler et al., 2004; Van Kranendonk et al., 2004) as well as physical (e.g. Dixon and Summers, 1983; Chardon et al., 1996) and numerical modeling (e.g. West and Mareschal, 1979; Mareschal and West, 1980; de Bremond d'Ars et al., 1999; Cagnard et al., 2006; Robin and Bailey, 2009; Thébaud and Rey, 2013). However, this important process, which is perhaps unique to the Archean, lack of studies integrating detailed metamorphic petrology and geochronology.

In order to better document the pressure–temperature–time (P–T–t) signatures of Archean domes we conducted a multidisciplinary study (structural, petrological, geochemical, geochronological and numerical) of the 3.5–3.2 Ga old Mount Edgar high-grade rocks of the East Pilbara Granite–Greenstone Terrane (EPGGT, Western Australia). This terrane displays narrow belts of strongly deformed greenstones (mafic to ultramafic volcanic rocks and metasediments), in association with broad TTG (Tonalite–Trondhjemite–Granodiorite) granitoids (Fig. S1). The Mount Edgar and

the Corunna Downs granitoids and the associated Warrawoona greenstone belt (Fig. 1) are considered one of the best documented examples of dome and basin structure interpreted to be formed by gravitational instability (e.g. Hickman, 1983, 1984; Collins, 1989; Teyssier et al., 1990; Delor et al., 1991; Collins, 1993; Collins et al., 1998; Van Kranendonk et al., 2004). Other interpretations include thrust stacking (e.g. Van Haaften and White, 1998), metamorphic core complex attending regional extension (e.g. Bickle et al., 1980, 1985; Boulter et al., 1987; Zegers et al., 1996; Van Haaften and White, 1998; Kloppenburg et al., 2001; Van Haaften and White, 2001), and complex folded structures formed during crustal shortening (Blewett, 2000, 2002) followed by channel flow (Harris et al., 2012).

The results of our multidisciplinary approach constrain the P–T–t evolution of the high-grade rocks from the Mount Edgar granitoid dome that documents the deep burial and exhumation of surface rocks. In addition, oxygen isotopes of zircons are used to investigate the nature of the protolith of the high-grade rocks. The P–T–t results are then compared with predictions from thermo-mechanical modeling of sagduction leading to insight into the tectonics of Archean dome and basin terranes.

2. Geological settings

The Eastern Pilbara Province (*ca.* 3.65–2.83 Ga) is characterized by dome and basin structures that are composed of large TTG domes (35–100 km in diameter), which intruded into a greenstone cover sequence (volcanic and sedimentary metamorphosed rocks) (Fig. S1). The greenstone sequence is divided into several Groups (Hickman, 1983, 1984). The Warrawoona Group (*ca.* 12 km thick) was deposited over a 100 Myr period as a result of continuous volcanism from 3530 to 3430 Ma. Voluminous TTG magmas produced at this stage (i.e. Callina and Tambina Supersuite) were emplaced at mid- to upper-crustal levels but not erupted to the surface (Van Kranendonk et al., 2002; Pawley et al., 2004; Smithies et al., 2007). Unconformably overlying the Warrawoona Group is the Kelly Group (<9 km thick), which was deposited between 3335 and 3312 Ma. The time gap of *ca.* 100 Myr preceding the deposition of the Kelly Group implies a hiatus in basaltic volcanism, during which the Warrawoona Group was uplifted and eroded (Buick et al., 1995; Van Kranendonk et al., 2002). The bottom of the Kelly Group consists of the Euro Basalt, which contains interbedded komatiitic and tholeiitic basalts that were erupted between 3350 and 3320 Ma. This was followed by eruption of the 3320 to 3310 Ma Wyman Formation and by the emplacement of voluminous granodioritic plutons of the Emu Pool Supersuite (3325–3290 Ma). Continuous basaltic volcanism until 3312 Ma led to the formation of the overlying Charteris Basalt (Hickman, 1984). The dominantly volcanic and sedimentary rocks of the 2770–2640 Ma Fortescue Group overlie the previous Groups and are separated from them by a regional unconformity.

Here, we focused our study on the southern part of the Mount Edgar granitic dome and adjacent Warrawoona Greenstone Belt (Fig. 1). The contact between these two entities is affected by a kilometric-scale shear zone with down-dip radial stretching lineations (Collins, 1989; Teyssier et al., 1990; Collins et al., 1998; Thébaud et al., 2008). In the granitic dome complex, older gneissic/orthogneissic components (3470–3430 Ma) are preserved along the outer margins of the dome, whereas younger (3330–3220 Ma) voluminous granodioritic phases are present in the dome core. These granodiorites are derived from partial melting of older gneisses (Williams and Collins, 1990; Bickle et al., 1993; Van Kranendonk et al., 2004), while older TTG derive from either mafic material (Smithies, 2000) or a crustal source (Bickle et al., 1993). The Mount Edgar dome emplacement occurred after the emplacement of the Warrawoona and the Kelly Groups (Collins et al., 1998; Kloppenburg, 2003). The Charteris Formation (top of the Kelly Group) dated between 3315 and 3312 Ma, and the absence of major unconformity between this formation and the underlying formations suggest that it was deposited prior to the initiation of deformation (Collins et al., 1998).

Previous work on the region has resulted in different interpretations of the tectonic evolution including diapirism (e.g. Collins, 1989; Williams and Collins, 1990; Delor et al., 1991; Collins, 1993; Collins et al., 1998; Collins and Van Kranendonk, 1999; Wellman, 2000; Van Kranendonk et al., 2001, 2002; Thébaud et al., 2006), tectonic models of thrust stacking (e.g. Van Haaften and White, 1998), core complex formation (Kloppenburg et al., 2001), and fold interference (Blewett, 2002). At the regional scale, the Warrawoona Greenstone Belt (Fig. 1) shows a dominating foliation that is steeply dipping and sub-parallel to the greenstone/granitoid boundaries. Regional map data from previous studies (e.g. Collins, 1989; Van Haaften and White, 1998; Thébaud et al., 2006) show that the Southern rim of the Mount Edgar is affected by a kilometer-scale shear zone and displays a radial pattern of metamorphic mineral elongation and/or stretching lineations. This is at odds with the interpretations made by Van Haaften and White (1998) and Kloppenburg et al. (2001) who describe the lineation as unidirectional and trending NE–SW. Kinematic analysis revealed that the shear zone accommodated the exhumation of the granitoid dome, resulting a 'Mount Edgar-up, greenstone-down' sense-of-shear (Collins, 1989; Teyssier et al., 1990; Collins et al., 1998).

Previous studies have shown that the greenstones are mainly characterized by a greenschist-facies metamorphic overprint, except near domes margins, where they reach amphibolite-facies conditions resembling contact metamorphism. Medium pressure ($\leq$6 kbar) assemblages containing kyanite and andalusite or sillimanite; kyanite has been described along the southwestern contact of Mount Edgar (Delor et al., 1991; Collins and Van Kranendonk, 1999; Le Hebel and Rey, 2005; Le Hebel et al., 2005). The amphibolite-facies overprint is attributed to the increased metamorphic conditions that occurred in a sinking greenstone keel (Collins and Van Kranendonk, 1999).

A large number of U–Pb zircon SHRIMP ages have been obtained throughout the Pilbara Granite–Greenstone Terrane (Fig. S2) (Pidgeon, 1978; Williams and Collins, 1990; Thorpe et al., 1992; Nelson, 1997; Collins et al., 1998; Nelson, 1998, 1999, 2001a, 2001b; Kloppenburg, 2003). Available ages are mainly for the granites of Mount Edgar and Corunna Downs. Zircon U–Pb ages have been obtained for rocks forming the Warrawoona Greenstone Belt including the felsic Duffer (3468 $\pm$ 2 Ma, Nelson, 2001b; 3449 $\pm$ 5 Ma, Thorpe et al., 1992) and Wyman (3315 $\pm$ 5 Ma, Pidgeon, 1978) Formations. At Mount Edgar, three main generations of granitic rocks have been described. The two oldest samples are gneisses on the southern and western margins belonging to the Callina (3490–3460 Ma) and the Tambina (3450–3420 Ma) Supersuites (Van Kranendonk et al., 2007). The third sample consists of a granodiorite located in the center of the dome and corresponding to the Emu Pool Supersuite (3325 and 3290 Ma) (Pidgeon, 1978; Williams and Collins, 1990; Thorpe et al., 1992; Collins et al., 1998; Kloppenburg, 2003) (Fig. S2). U–Pb ages on the gneissic margins range between 3465 and 3429 Ma, which suggests that the oldest TTGs were emplaced at about the time when part of the Warrawoona Group sediments and volcanic sequences were deposited (3508–3445 Ma) (Hickman, 1983). Similar ages for the core of Mount Edgar and Corunna Downs indicates synchronous formation of these two domes. Their emplacement postdates the deposition of the Warrawoona Group (Collins et al., 1998; Kloppenburg, 2003). The presence of a small, non-foliated granitic pluton (Wilina Pluton), located on the SE sheared margin of Mount Edgar, and dated at 3324 $\pm$ 6 Ma, constrains a minimum age for the initiation of deformation (Collins et al., 1998). Ar/Ar ages of amphiboles from the

dome and the Warrawoona Greenstone Belt range between 3325 and 3300 Ma (Kloppenburg, 2003) (Fig. S2). These ages probably represent resetting during intrusion and related metamorphism as Ar–Ar in hornblende amphibole resets at about 500–550 °C (Dallmeyer, 1978; Harrison, 1982). Ar/Ar ages on muscovite between 2894 ± 8 Ma and 2801 ± 19 Ma have been attributed to a reopening of these minerals due to a second, lower thermal event (Ar–Ar closure temperature of muscovite is generally considered to be between 400–450 °C; Harrison et al., 2009).

3. Sample descriptions

A variety of garnet-bearing metasediments and metabasalts along the SW and SE rims of the Mount Edgar Dome, as well as a metasedimentary enclave located inside the dome (Fig. 1).

3.1. SW Mount Edgar margin, Chinaman shear zone

A staurolite-garnet-bearing felsic schist from the base of the Warrawoona Group (Duffer Formation 3471–3463 Ma) was collected south of the Chinaman shear zone towards the SW margin of the Mount Edgar granitic complex (Fig. 1). This sample is characterized by a strong foliation, locally refolded, and striking NW–SE and strongly dipping towards the SW (Kloppenburg et al., 2001; Thébaud et al., 2006). This foliation carries a stretching lineation plunging to the WSW. The orientation of axial planes of the folds suggests a NE–SW shortening that is likely related to the emplacement of the granitoid dome. The occurrence of staurolite and garnet in this sample testifies to amphibolite-facies conditions. The progressive disappearance of staurolite and garnet and formation of albite and chlorite towards the south indicates a metamorphic transition from amphibolite to greenschist-facies conditions (Teyssier et al., 1990; Delor et al., 1991; Collins et al., 1998).

PB-11-13 is a metasediment containing abundant, large garnet crystals (100 µm to 5 cm in diameter), surrounded by a muscovite–staurolite–andalusite–chlorite–quartz matrix. Garnet is strongly sheared and displays a dominantly top to the SW sense of shear (Fig. 2a) underlined by a muscovite-bearing stretching lineation. Staurolite is found both as a matrix phase and as primary inclusion in garnet (Fig. 3d), which also contains monazite inclusions in the core (Fig. 5b, see monazite ages below). Other mineral inclusions present in garnet are staurolite, quartz, muscovite, biotite, apatite, ilmenite and rutile.

3.2. Metasedimentary enclave in the Mount Edgar dome

The Mount Edgar consists of an older gneissic component (*ca.* 3.469–3.430 Ga) exposed on the southern and western margins of the dome, and a younger granodioritic component (*ca.* 3.324–3.290 Ga). The granodiorite contains enclaves of felsic, mafic and ultramafic rocks that were equilibrated under greenschist- to granulite-facies conditions. The enclaves and host granitoid show the same NE–SW trending foliation and SE plunging stretching lineation, thus indicating that they experienced the same late deformation history. Petrological and geochronological data have been obtained on three samples collected from a 50 × 100 meter felsic enclave (Fig. 2c).

PB-11-23 is a strongly deformed metatexite containing anhedral porphyroblasts of almandine-rich garnet (X_{Alm} 0.74–0.77; Figs. 2c and 3a). The surrounding matrix is composed of fibrolite sillimanite, quartz, biotite, plagioclase and minor K-feldspar (Fig. 3a1). Garnet contains inclusions of muscovite, sillimanite, biotite, with minor ilmenite and zircon. The absence of muscovite in the rock matrix and presence in the garnet core argue for an early, lower-grade metamorphic stage coeval or pre-dating garnet growth. *PB-11-28* is a garnet-free leucosome layer composed of sillimanite, quartz, biotite and minor zircon (Fig. 3b). *PB-11-27* is a restitic layer containing large crystals of garnet, biotite, plagioclase, K-feldspar and zircon (Fig. 3c).

All three samples contains small zircons (20 to 100 µm) displaying a variety of shapes from rounded to euhedral. Zircons contain inclusions of sillimanite, biotite, plagioclase, K-feldspar and monazite (Fig. 5a).

3.3. SE Mount Edgar margin at Trig well

This area consists mainly of deformed, amphibolite-facies mafic and felsic schists of the Duffer Formation.

PB-11-33 is an aluminosilicates-bearing schist (Fig. 2b) containing andalusite and kyanite (locally reequilibrated into pyrophyllite and chlorite) within a matrix of white mica and quartz (Fig. 3e). Kyanite occurs as inclusions in andalusite, thus arguing for its primary nature. The main stretching lineation is underlined by muscovite. Microstructural analysis indicates mainly top to the SE sense of shear (Fig. 3e).

PB-11-35 is a garnet-bearing schist consisting of garnet, biotite, quartz and minor muscovite, staurolite and chlorite. Staurolite is present in the matrix and as inclusions in garnet. Garnet shows internal sigmoidal features underlined by elongated quartz and staurolite inclusions, which indicate that it formed in part during shearing. The stretching mineral lineation is defined by biotite.

PB-11-36 is a mafic schist composed of garnet porphyroblasts, hornblende and epidote embedded in a matrix of chlorite, biotite, hornblende and plagioclase (Fig. 3f). Garnets are large, automorph and syn-tectonic as attested by internal sigmoidal features underlined by mineral inclusions.

4. Analytical methods and modeling approaches

4.1. Thermobarometry and thermodynamic modeling

In order to characterize the metamorphic events and to constrain the *P*–*T* conditions both inside and outside the dome, we performed a metamorphic and thermobarometric study. All mineral compositions used for thermobarometry were obtained using a Cameca SXFive installed at CAMPARIS, University Pierre & Marie Curie, Paris. Operating conditions were 15 kV and 10 nA for most minerals. Whole-rock chemistry of the samples were obtained at the Service d'Analyse des Roches et Minéraux (CRPG, Nancy) by ICP-OES (major elements) and ICP-MS (trace elements) using the techniques described in Carignan et al. (2001). Whole rock compositions are given in Table 1.

The different methods used to constrain the *P*–*T* conditions are as follows:

1) A multi-equilibria approach using the WinTWEEQU software based on the thermodynamical data of Berman (1988) and the solution properties of garnet (Berman, 1990), biotite (McMullin et al., 1991), white mica (Chatterjee and Froese, 1975), amphibole (Mäder et al., 1994) and plagioclase (Fuhrman and Lindsley, 1988).

2) Thermodynamic modeling using the phase-diagram calculation software Perple_X (version 6.6.8.) (Connolly, 1990) and the self-consistent themodynamic database and mineral solution models (solution_model) of Holland and Powell (1998, upgrade 2002). Bulk-rock compositions were calculated in the MnNaCaKFMASH system from modal phase proportions. Water and quartz were considered to be in excess for *P*–*T* pseudosections except for sample PB-11-23 (which contains partial melt), for which the H_2O content was estimated using an xH_2O *vs* temperature (at constant pressure) diagram. Pseudosections were constructed for conditions between 400 and 900 °C, and between 3 and 13 kbar. Isopleths of garnet, biotite and white mica were also constructed to specify and refine the conditions of metamorphic peak. Results for all samples are shown in Fig. 4.

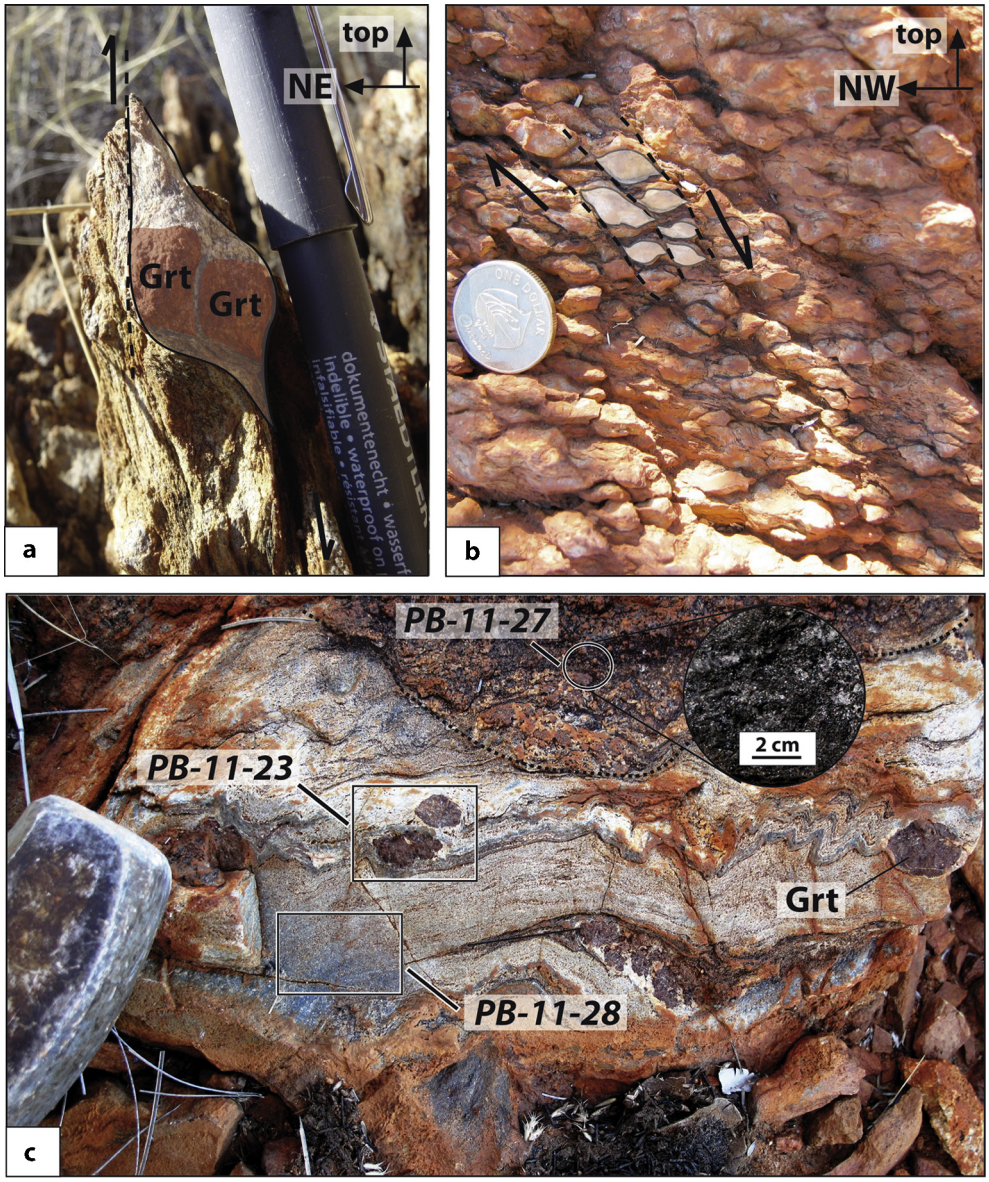

Fig. 2. (a) *Sample PB-11-13*: garnet metasediment in muscovite-quartz matrix. *SW dome rim*, shearing top-to-the SW. Picture is parallel to the stretching lineation and normal to the foliation. (b) *Sample PB-11-33*: aluminosilicate schist, *SE dome rim*, shearing top-to-the SE. Sections are parallel to the stretching lineation and normal to the foliation. (c) Metasedimentary enclave in Mount Edgar dome showing alternating leucosome layers with large garnets (*sample PB-11-23*) and garnet-free (*sample PB-11-28*), and restitic layers (*sample PB-11-27*) with large and abundant biotite. All mineral abbreviations are from Kretz (1983).

4.2. U–Pb geochronology and oxygen isotopes

In order to constrain the age of metamorphism in rocks from the margin and center of the dome, three samples of metasedimentary enclaves (PB-11-23 and PB-11-28 from the dome center and PB-11-13 from the SW margin) were selected for in situ U–Th–Pb dating on zircon and monazite. Rock samples were crushed using a tungsten jaw crusher. Mineral separation involved the use of heavy liquids (lithium metatungstate and methylene iodide) and a Frantz magnetic separator.

Zircons were handpicked, mounted in epoxy resin and polished to exposed grain centers. Part of the thin section of cm-scale garnet with monazite inclusions (PB-11-13, Fig. 5b) was also mounted in epoxy to allow *in-situ* dating. Analyses were performed at the Research School for Earth Sciences, the Australian National University, Canberra. The internal structures of zircons and monazite grains was investigated with back scattered electron (BSE) and cathodoluminescence (CL) images that were acquired with a JEOL JSM 6610-A scanning electron microscope at 15 kV and ~10–20 mm working distance. Mineral inclusions in the grains were determined using an Energy Dispersive Spectrometer (EDS) attached to the same instrument.

U–Pb analyses were performed using the sensitive high resolution ion microprobe (SHRIMP II) at the Australian National University in Canberra. Instrumental conditions and data acquisition were generally as described by Williams (1998). The measured $^{206}Pb/^{238}U$ ratio was corrected using an igneous zircon reference material (OG1, 3465 Ma, Stern et al., 2009, or TEM, 417 Ma, Black et al., 2003) and reference monazite from Thompson Mine, Manitoba, Canada (TM, 1766 Ma). Data were corrected for common Pb on the basis of the measured ^{204}Pb as described in Williams (1998). The data were treated following the SQUID and Isoplot programs of Ludwig (2001). Ratios and ages for individual analyses are given with 1σ error, whereas average ages are given at 95% confidence level. Geochronological data are presented in Table 2 (PB-11-23 and PB-11-27) and Table 3 (PB-11-13).

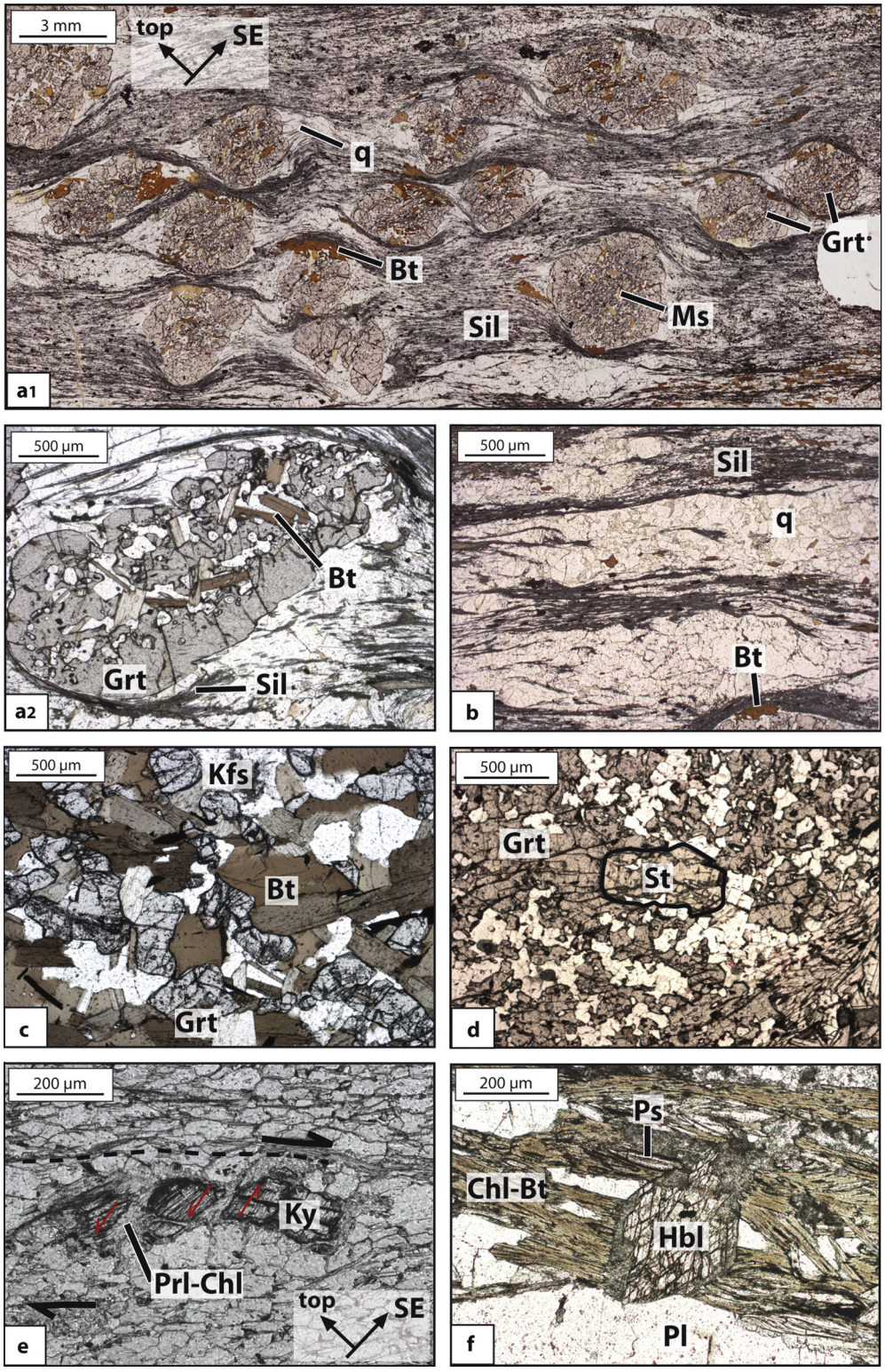

Fig. 3. Photomicrographs (a1) *Sample PB-11-23* (*enclave in Mount Edgar dome*): sheared garnets (SE-down dominant) with inclusions of muscovite, biotite, quartz and sillimanite, in a matrix of sillimanite fibrolite, quartz and biotite. (a2) *Sample PB-11-23*: leucosome layer with porphyroblast of garnet. (b) *Sample PB-11-28*, leucosome layer garnet-free: matrix with abundant sillimanite and quartz, and some biotite. (c) *Sample PB-11-27, restitic layer*: large crystals of biotite, garnet and K-feldspar. Sillimanite is absent. (d) *Sample PB-11-13* (*SW margin of Mount Edgar*) showing an inclusion of staurolite grain in a garnet. (e) *Sample PB-11-33* (*SE margin of Mount Edgar*): pyrophyllite–chlorite partial pseudomorph after kyanite. Shearing is SE down and antithetic microfractures. (f) *Sample PB-11-36* (*SE margin of Mount Edgar*): secondary chlorite after hornblende in matrix containing pistachite, hornblende, plagioclase and late biotite and chlorite. All sections are parallel to stretching lineations and normal to foliation.

Table 1
Whole-rock analyses of the Mount Edgar south metasediments and metabasalt.

Sample:	PB-11-13	PB-11-23	PB-11-33	PB-11-35	PB-11-36
Rock Type:					
SiO_2	62.46	68.64	78.34	65.70	53.61
TiO_2	0.95	1.47	0.43	0.96	0.73
Al_2O_3	17.15	20.97	17.72	15.10	15.95
Fe_2O_3	8.71	5.72	0.17	6.68	10.61
MnO	0.51	0.16	0.01	0.18	0.24
MgO	1.95	0.77	0.10	2.88	6.06
CaO	0.72	0.46	0.07	1.84	5.44
Na_2O	0.39	0.30	0.35	1.85	0.71
K_2O	3.09	0.91	0.61	2.19	1.79
P_2O_5	0.21	0.07	0.14	0.19	0.04
LOI	3.10	0.69	1.72	1.74	3.93
Total	99.22	100.15	99.70	99.28	99.10

Analyses performed at the SARM CRPG-Nancy by ICP-OES (major elements) and ICP-MS (trace elements) using techniques described in Carignan et al. (2001).

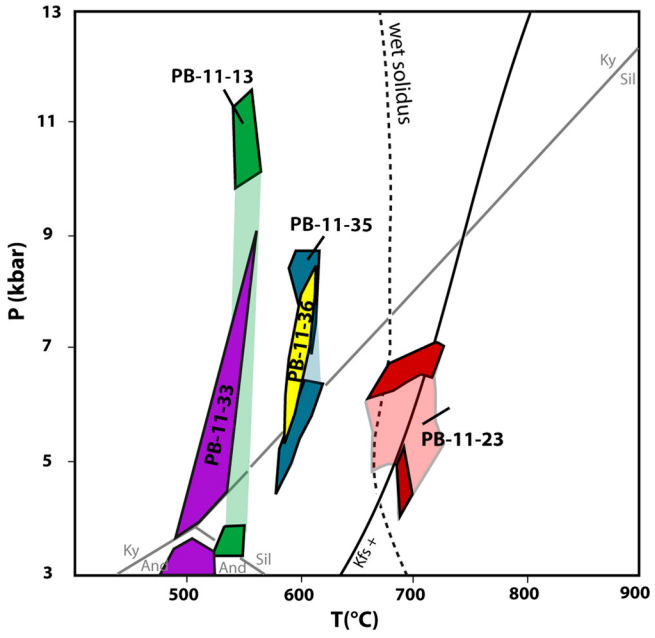

Fig. 4. P–T diagram with compilation of thermobarometric results of Perple_X pseudosections; each box corresponds to a sample, the Kfs + line corresponds to the appearance and the disappearance of K-feldspar.

A separate analytical session on the same instrument was run to establish the oxygen composition of zircons and garnets in samples PB-11-23 and PB-11-28, in order to constrain the protolith of the enclave. Analytical set followed that of Ickert et al. (2008) for zircon. Temora zircon (TEM, $\partial^{18}O = 8.2‰$, Black et al., 2003) was used as reference material. Garnet analyses followed the procedure described by Martin et al. (2014) using UWG2 garnet as standard. A matrix bias correction for the grossular and spessartine component of garnet was applied following the equation given in Martin et al. (2014). The garnet composition was based on EDS analyses with the JEOL JSM 6610-A scanning electron microscope. Errors on the individual oxygen analyses and on the average values are given at 2σ and 95% confidence limit, respectively. They include the error on the reproducibility of the standard in the same session, and, in the case of garnet, that of the matrix correction ($\pm 0.25‰$, 1σ). Oxygen isotope results are presented in Table ST1 and ST2, and in Fig. S4.

4.3. Thermo-mechanical modeling

In order to interpret metamorphic data in terms of tectonic processes, we carried out a series of 2D coupled thermo-mechanical experiments to compare and contrast our metamorphic data with the range of P–T–t paths followed by high- to medium-grade rocks during sagduction. For the modeling we used Ellipsis (Moresi et al., 2001, 2002), a particle-in-cell code capable of handling viscoplastic rheologies. We adopted a realistic geotherm with intrinsic-radiogenic heating and mantle heat-flow appropriate for the Archean. Importantly, the code takes into account partial melting with feedback on densities and viscosities. For the continental crust we imposed a solidus and a liquidus defined as polynomial function of temperature. We do not try to match the solidus and liquidus of any specific crustal lithology. Instead, the position of the solidus and liquidus in P–T space were adjusted to obtain a melt fraction of <35%. Viscosities decrease of three orders of magnitude as the melt fraction increases from 0.2 to 0.3. In nature, the viscosity drops by many orders of magnitude (Clemens and Petford, 1999), however only the first two or three orders of magnitude are likely to have mechanical significance. As the temperature increases from the solidus to the liquidus, the density of the partially melted region decreases by 13%, which in turn increases its buoyancy.

Our numerical experiments (Fig. 7) involve a 15 km thick greenstone cover (2840 kg m^{-3}) on top of a 30 km thick sialic protocrust (2720 kg m^{-3}). Densities are constrained by gravity modeling in EPGGT (Blewett et al., 2004). The thickness of the greenstone cover is compatible with that of the Warrawoona and Kelly Groups in the Eastern Pilbara (e.g. Van Kranendonk et al., 2007). In the model, the greenstone cover is emplaced in four successive layers (*ca.* t_0, $t_0 + 30$ Myr, lower Warrawoona Group, $t_0 + 60$ Myr, upper Warrawoona Group, and $t_0 + 140$ Myr, Kelly Group), as described in Thébaud and Rey (2013), to approximate the emplacement history of the greenstone cover. The thickness of the greenstone cover is laterally inhomogeneous with variation of thicknesses (up to 2.5 km) to help the initiation of sagduction. Such a lateral variations in thickness could be due to rapid accumulation of effusive rocks on the surface, causing the flow of the deep crust (e.g. Flament et al., 2011), or to normal faulting coeval with volcanism. The initial geotherm was calculated assuming a basal heat flow of 25 mW m^{-2} and a crustal radiogenic heat production determined at 3.5 Ga from present-day averaged radiogenic content of Archean crust (Taylor and McLennan, 1986). The standard viscoplastic rheological profile of Brace and Kohlstedt (1980) for the continental lithosphere was used. The plastic flow is described by a Mohr–Coulomb type failure law, augmented by a strain-dependent weakening function $f(\varepsilon)$ that simulates damage-related strain localization. The frictional faulting is described by a yield stress: $\sigma_{\text{yield}} = (\sigma_n \tan(\phi) + C_0) f(\varepsilon)$, where σ_n is the normal stress, ϕ is the angle of internal friction and C_0 is the cohesion. Strain localization is achieved by the strain weakening function $f(\varepsilon)$, which reduces the yield stress as the accumulated strain (ε) increases. The strain weakening function is defined by:

$$f(\varepsilon) = \begin{cases} 1 - (1-a)(\varepsilon/\varepsilon_0)^n & \text{when } \varepsilon < \varepsilon_0 \\ a & \text{when } \varepsilon \geq \varepsilon_0 \end{cases}$$

where ε is the accumulated strain, and ε_0 is the threshold strain from which the yield stress is reduced by an amount a. The stress exponent n modulates the dependency between accumulated strain and strain weakening. The viscous rheology for the crust includes both diffusion and dislocation creeps (Bürgmann and Dresen, 2008). For the mantle, diffusion creep is disregarded. Both creep regimes can be described by Arrhenius approximation of viscosity (Karato and Wu, 1993).

$$\eta = \left(\frac{1}{2A^{(\frac{1}{n})}}\right) . e^{(\frac{Q}{nRT})} . \dot{\varepsilon}^{(\frac{1-n}{n})}$$

Where A is the pre-exponential factor in the power law (see Brace and Kohlstedt, 1980, Table 1), n the power law stress exponent,

Table 2
SHRIMP zircon U–Th–Pb isotope data for the core of the Mount Edgar granulitic metasediments.

Spot name	^{206}Pbc (%)	U (ppm)	Th (ppm)	Th/U	$\frac{^{207}Pb}{^{235}U}$	1σ err (%)	$\frac{^{206}Pb}{^{238}U}$	1σ err (%)	err corr	$\frac{^{207}Pb}{^{206}Pb}$	1σ err (%)	$\frac{^{207}Pb}{^{206}Pb}$ age (Ma)	1σ err	%Disc	Domain
23.4.1	0.12	78	5.1	0.066	25.49	1.4	0.6832	1.2	0.86	0.2706	0.70	3309.3	11.0	−1.4	–
23.4.2	0.05	103	7.1	0.069	25.01	1.8	0.6713	1.7	0.95	0.2702	0.53	3306.9	8.3	−0.1	–
23.5.1	0.09	112	2.8	0.025	24.42	1.2	0.6535	1.1	0.90	0.2710	0.51	3311.8	8.0	2.2	–
23.5.2	0.04	86	2.1	0.024	25.53	1.3	0.6915	1.1	0.89	0.2678	0.58	3293.2	9.0	−2.8	–
23.5.3	0.05	106	2.8	0.026	25.24	1.3	0.6732	1.1	0.90	0.2720	0.56	3317.3	8.7	0.0	–
23.5.4	0.35	161	2.2	0.014	26.31	1.3	0.7108	1.1	0.86	0.2685	0.65	3297.1	10.0	−4.8	–
23.5.5	0.13	102	2.1	0.020	24.67	1.2	0.6649	1.1	0.90	0.2691	0.54	3301.0	8.5	0.5	–
23.5.6	0.16	133	1.7	0.013	24.49	1.3	0.6574	1.2	0.92	0.2702	0.51	3307.4	8.0	1.5	–
23.5.7	0.10	125	1.8	0.014	25.25	1.4	0.6784	1.3	0.94	0.2700	0.47	3306.1	7.3	−1.0	–
23.5.8	0.07	112	1.4	0.013	24.70	1.2	0.6608	1.1	0.91	0.2711	0.49	3312.6	7.7	1.3	–
23.6.1	0.09	95	7.5	0.079	25.53	1.3	0.6810	1.1	0.85	0.2719	0.71	3316.8	11.0	−0.9	–
23.1	0.19	77	4.8	0.063	24.70	1.8	0.6630	1.7	0.96	0.2702	0.51	3307.4	7.9	0.9	–
23.2	0.06	102	5.4	0.053	23.93	1.7	0.6421	1.7	0.97	0.2702	0.42	3307.4	6.6	3.4	–
23.3	0.04	149	7.6	0.051	24.97	1.6	0.6674	1.6	0.98	0.2714	0.34	3314.1	5.3	0.6	–
23.4	0.00	160	7.9	0.050	25.95	1.7	0.6940	1.6	0.97	0.2712	0.43	3312.9	6.8	−2.5	–
23.5	0.04	313	11.9	0.038	23.76	2.2	0.6296	2.1	0.99	0.2737	0.24	3327.4	3.7	5.7	–
23.6	0.06	147	11.7	0.080	23.65	1.7	0.6293	1.7	0.95	0.2726	0.53	3321.1	8.3	5.5	–
23.7	0.10	121	10.6	0.088	23.79	1.7	0.6436	1.6	0.97	0.2681	0.39	3295.0	6.2	2.9	–
23.8	0.13	122	5.2	0.043	24.40	1.7	0.6537	1.7	0.97	0.2707	0.41	3310.0	6.5	2.1	–
28.1	0.10	2844	5.1	0.002	2.624	1.5	0.1719	1.5	0.97	0.1107	0.40	1811.7	7.2	77	rim
28.2	0.04	1314	10.7	0.008	9.182	1.6	0.3211	1.6	0.98	0.2074	0.32	2885.1	5.1	61	rim
28.3	0.03	2337	1.6	0.001	2.544	1.5	0.1729	1.5	0.98	0.1067	0.27	1744.2	4.9	70	rim
28.4	0.04	2068	0.3	0.000	11.28	1.6	0.3533	1.5	0.95	0.2316	0.50	3062.8	8.0	57	rim
28.5	0.02	1078	6.3	0.006	12.48	1.6	0.3937	1.5	0.97	0.2298	0.36	3050.8	5.8	43	rim
28.6	0.05	2369	10.8	0.005	2.738	1.5	0.1715	1.5	0.98	0.1158	0.28	1893.0	5.0	86	rim
28.7	0.17	2139	7.6	0.004	3.183	1.6	0.1805	1.6	0.97	0.1279	0.43	2069.4	7.5	93	rim
28.8	0.18	1909	9.3	0.005	4.565	2.3	0.2093	1.5	0.66	0.1582	1.72	2436.9	29.0	99	rim
28.9	0.02	854	16.3	0.019	21.21	2.1	0.5854	2.1	1.00	0.2628	0.16	3263.6	2.5	10	rim
28.11	0.12	1685	3.3	0.002	4.463	1.5	0.2112	1.5	0.98	0.1533	0.29	2382.5	5.0	93	rim
28.12	0.06	1544	5.9	0.004	7.020	1.5	0.2717	1.5	0.99	0.1874	0.21	2719.6	3.5	76	rim
28.13	0.08	2096	6.7	0.003	6.965	1.7	0.2633	1.5	0.90	0.1918	0.74	2758.0	12.0	83	rim
28.10	0.03	212	7.7	0.036	25.14	1.7	0.6722	1.6	0.98	0.2713	0.34	3313.4	5.3	0.0	core
28.14	0.05	160	10.6	0.066	26.57	1.7	0.7121	1.7	0.97	0.2706	0.45	3309.5	7.0	−4.5	core
28.15	0.00	153	6.5	0.043	24.83	1.7	0.6610	1.6	0.98	0.2725	0.35	3320.2	5.5	1.5	core
28.17	0.05	88	5.1	0.058	25.01	1.8	0.6694	1.7	0.96	0.2709	0.46	3311.4	7.2	0.2	core
28.18	0.10	103	7.6	0.074	27.04	1.8	0.7166	1.7	0.96	0.2737	0.50	3327.3	7.9	−4.5	core
28.19	0.03	87	6.5	0.075	24.13	1.8	0.6469	1.7	0.96	0.2705	0.51	3309.1	8.0	2.9	core
28.20	0.07	88	9.2	0.105	23.33	1.7	0.6238	1.7	0.96	0.2713	0.46	3313.4	7.3	6.0	core
28.21	0.11	88	7.4	0.085	25.23	1.8	0.6737	1.7	0.94	0.2716	0.59	3315.6	9.3	−0.1	core
28.22	0.07	88	9.8	0.112	25.03	1.7	0.6652	1.7	0.96	0.2729	0.46	3322.6	7.2	1.1	core
28.23	0.03	104	5.9	0.057	25.55	2.5	0.6845	2.5	0.98	0.2707	0.46	3310.1	7.1	−1.5	core
28.24	0.03	111	14.0	0.126	25.25	1.7	0.6747	1.6	0.97	0.2714	0.40	3314.2	6.3	−0.3	core
28.25	0.03	122	6.5	0.054	24.45	1.9	0.6535	1.9	0.98	0.2713	0.38	3313.7	5.9	2.2	core
28.26	0.03	107	8.0	0.075	25.23	1.7	0.6704	1.7	0.97	0.2729	0.44	3322.8	6.9	0.5	core
28.27	0.02	126	6.5	0.051	23.69	1.7	0.6363	1.7	0.97	0.2701	0.41	3306.4	6.4	4.2	core
28.28	0.03	87	11.7	0.134	24.64	1.7	0.6555	1.7	0.96	0.2726	0.46	3321.3	7.2	2.2	core
28.30	0.07	96	9.2	0.096	25.52	1.7	0.6860	1.7	0.97	0.2698	0.44	3304.7	6.9	−1.9	core

Pbc denotes the common lead and ages are ^{204}Pb corrected.

Table 3
SHRIMP monazite U–Th–Pb isotope data for margins of the Mount Edgar metasediments.

Spot name	^{206}Pbc (%)	U (ppm)	Th (ppm)	Th/U	$\frac{^{207}Pb}{^{235}U}$	1σ err (%)	$\frac{^{206}Pb}{^{238}U}$	1σ err (%)	err corr	$\frac{^{207}Pb}{^{206}Pb}$	1σ err (%)	^{207}Pb/^{206}Pb age (Ma)	1σ err	%Disc
MON-05	0.010	948	15815	16.69	28.22	1.1	0.6948	1.1	0.96	0.2946	0.33	3442.2	5.1	1
MON-10-1	0.008	2453	35752	14.57	29.49	1.1	0.7278	1.0	0.92	0.2939	0.42	3438.2	6.5	−2
MON-10-2	0.073	432	8758	20.28	32.20	1.7	0.7888	1.6	0.93	0.2961	0.60	3449.9	9.3	−8
MON-12-1	0.000	872	20861	23.93	28.97	1.4	0.7152	1.2	0.84	0.2938	0.78	3437.9	12.0	−1
MON-12-2	0.055	894	16892	18.90	29.25	1.3	0.7148	1.2	0.94	0.2968	0.43	3453.6	6.6	−1
MON-14	0.010	787	20946	26.61	29.04	1.3	0.7109	1.2	0.88	0.2963	0.62	3451.0	9.7	0
MON-40	0.013	766	17325	22.63	28.26	2.0	0.7010	2.0	0.98	0.2924	0.40	3430.3	6.2	0
MON-42	0.014	1048	10329	9.850	27.55	1.9	0.6742	1.8	0.96	0.2963	0.54	3451.2	8.3	4
MON-46	0.010	1018	31237	30.68	30.15	1.3	0.7414	1.2	0.96	0.2950	0.38	3444.1	5.9	−4
MON-48	0.009	1602	27532	17.19	29.94	1.6	0.7356	1.5	0.94	0.2952	0.56	3445.5	8.6	−3

Pbc denotes the common lead and ages are ^{204} Pb corrected.

Q the activation energy of the creep mechanism, R the gas constant, T the temperature and $\dot{\varepsilon}$ the second invariant of the deviatoric strain rate tensor.

In addition, for computational efficiency, the viscosity range is limited between 5×10^{23} and 1×10^{18} Pa s. A free-slip boundary condition is used in all sides and no velocity condition is imposed

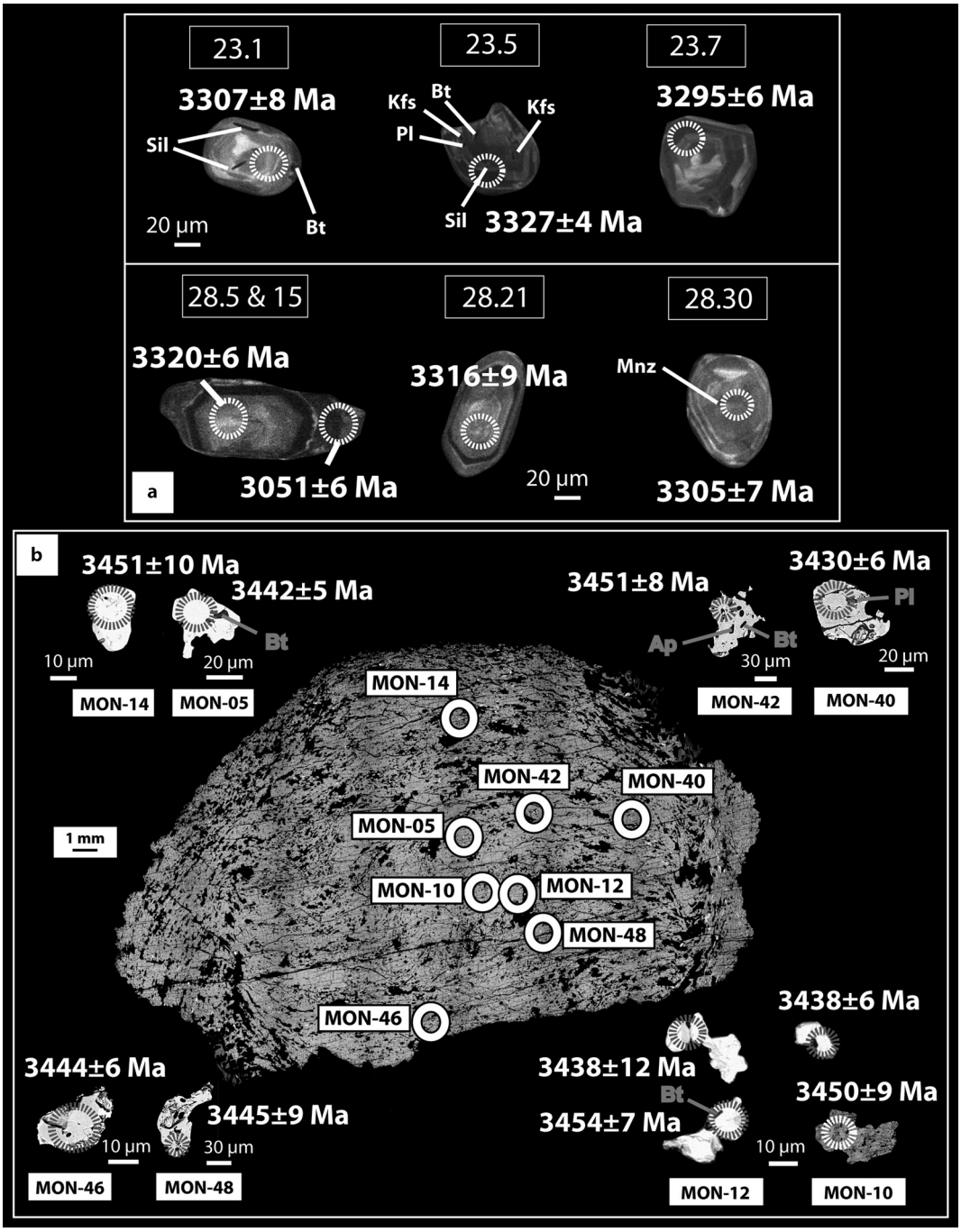

Fig. 5. (a) Cathodoluminescence images of selected zircons from the metasedimentary enclave in Mount Edgar dome (samples PB-11-23 and PB-11-28). Circles show SHRIMP II $^{207}Pb/^{206}Pb$ spot ages. (b) Backscattered electron imaging of a large garnet (2.5 × 1.5 mm, PB-11-13) and location of monazite inclusions. Dashed gray circles show the location of SHRIMP II analyses.

anywhere in the model. Additional details on the model are in Thébaud and Rey (2013).

To maintain rafts of greenstone at the surface, as it is observed in many Archean cratons, a strong strain weakening reduces the coefficient of friction from 0.268 to 0.01 when the accumulated plastic deformation reaches 15%. Without this strong strain weakening, the entire greenstone cover tends to sink into the lower crust. This brittle/plastic strength reduction could be caused by the presence of percolating fluids and/or melts along fractures, and thus decreasing friction coefficient of solid phases (Keller et al., 2013; Dymkova and Gerya, 2013).

5. Results

5.1. Petrology and thermobarometry

All samples contain a kyanite, garnet, muscovite, staurolite or amphibole mineral assemblage that is characteristic of mid-crustal metamorphic conditions. The oldest paragenesis is preserved within garnet (Figs. 3a and d). In PB-11-23, the presence of muscovite, plagioclase, sillimanite and biotite inclusions within garnet yielded P–T conditions of equilibration of 7 kbar and 650–700 °C (Fig. S3a). C/S bands and garnet rotation are associated

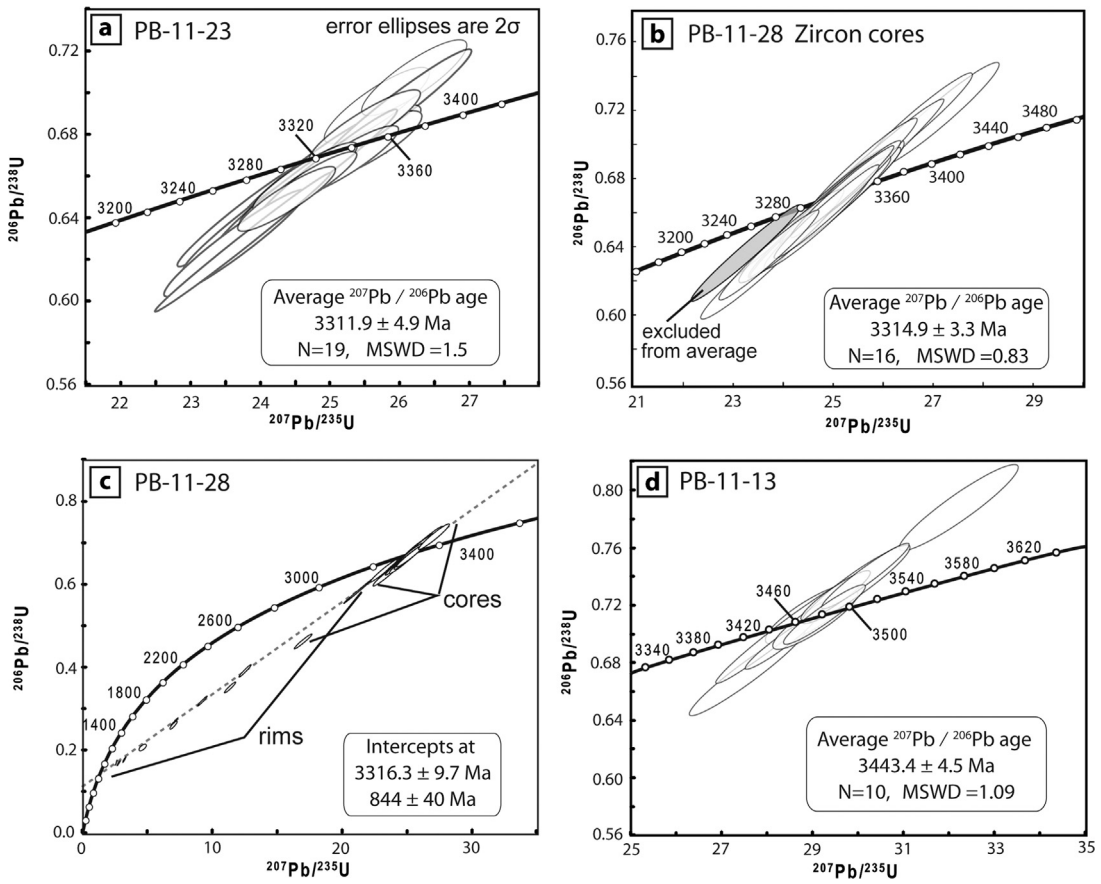

Fig. 6. Concordia diagrams for SHRIMP U–Th–Pb analyses of zircons and monazites in the different samples. (a) PB-11-23: U–Th–Pb analyses on 19 zircons. (b) PB-11-28: U–Th–Pb analyses on 16 zircon cores. (c) PB-11-28: U–Th–Pb analyses on 16 zircon cores and on 10 zircon rims. (d) Large garnet (PB-11-13): U–Th–Pb analyses on 10 monazites. Error ellipses are 2σ.

with a later stage paragenesis consisting of garnet, biotite, sillimanite, plagioclase and K-feldspar, which indicates P–T of equilibration of about 5 kbar and 600–670 °C (Fig. S3a). This stage corresponds to the breakdown of muscovite, now preserved as mineral inclusions in garnet, and the growth of biotite and K-feldspar. Such a rock composition together with its relatively high water content (H_2O = 2.7%) could have favored melting at relatively low temperatures (650–700 °C). Estimates of P–T conditions using different methods (Perple_X and classical thermobarometry) show similar and coherent results (Fig. S3b). The maximum pressure is around 7–11 kbar with a relatively large temperature range of 500–800 °C. Similar results (6–10 kbar, <750 °C) were obtained by Delor et al. (1991), Collins and Van Kranendonk (1999) and Le Hebel et al. (2005) for samples collected in the SW margin of the Mount Edgar dome. It is worth noting a progressive decrease of temperature from the dome core (sample PB-11-23, partially melted) towards its margins (sample PB-11-33) (Fig. 4, location in Fig. S1).

5.2. U–Pb geochronology and oxygen isotopes

5.2.1. Felsic sedimentary enclave

In sample PB-11-23, zircons show a weak oscillatory zoning. 19 analyses returned a tight cluster of concordant dates with a $^{207}Pb/^{206}Pb$ average at 3311.9 ± 4.9 Ma (MSWD = 2.1, Fig. 6a). Zircons show systematically low Th/U (0.01–0.09) regardless of the variable amounts of U (77–313 ppm) and Th (1–12 ppm) (Table 2). The oxygen isotope composition was measured on a subset of crystals in the same location as the U–Pb analysis. The average $\partial^{18}O$ value of zircons is 12.9 ± 0.3‰ (Fig. S4 & Table ST1). The oxygen isotope composition of garnet was measured across a large crystal in thin section. A 100 to 500 µm thick zone with brighter BSE emission indicative of a difference in composition is present along garnet rims and fractures that cross cut the grain. These brighter zones have a higher Mn content (X_{Sps} 0.05–0.08) and slightly lower $\partial^{18}O$ values (11.91 ± 0.55 ‰; Table ST2) than the inner part of the garnet (X_{Sps} 0.04–0.05 and $\partial^{18}O$ of 12.67 ± 0.58 ‰).

In sample PB-11-28, zircons show two distinct domains that differ in CL zoning, age, U–Th and oxygen composition. Zircon cores are similar to those of sample PB-11-23: they display weak oscillatory zoning, inclusions of metamorphic minerals and low Th/U ratio (0.04–0.13, Table 2). U–Pb analyses of the cores are mostly concordant and yield an average $^{207}Pb/^{206}Pb$ age at 3314.6 ± 3.3 Ma (MSWD 1.5) (Fig. 6b). A sub-set of zircons also have a rim darker in CL which is significantly richer in U (850–2840 ppm) than the cores (87–250 ppm) and has comparably low Th content (0.3–16 ppm) resulting in a particularly low Th/U ratio of 0.02–0.001. Zircon ages obtained in the rims are discordant and, when combined with the ages obtained in the cores, define a poorly-constrained Discordia with a lower intercept at 844 ± 40 Ma (MSWD 7.2) (Fig. 6c). The average $\partial^{18}O$ of the zircon cores is 13.1 ± 0.2‰, within error of the values obtained for sample PB-11-23. In contrast, zircon rims show significantly lower $\partial^{18}O$ values between 8.7 and 4.3‰ (Fig. S4 and Table ST1).

5.2.2. Dome margin sample

The large garnet of sample PB-11-13 contains inclusions of monazite (Fig. 5b). Zircons were not observed in this sample. The monazite grains are relatively small (20–50 µm) and do not show any zoning pattern in BSE imaging. Monazites contain rare inclusions of biotite, plagioclase, quartz and apatite, which are not

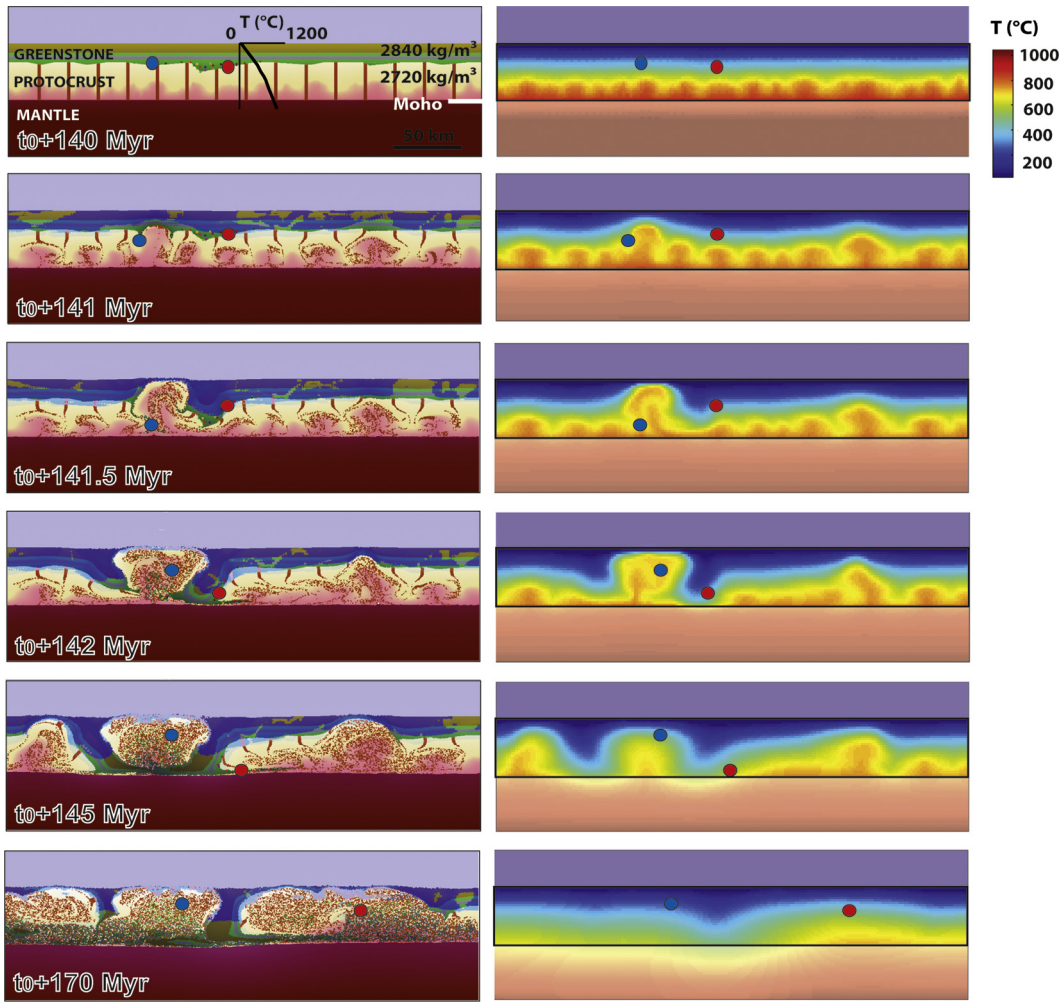

Fig. 7. Model geometry through time (left panel) and relative thermal history (right panel). Top left box shows initial setting after 140 Ma of flood basalt accumulation and thermal relaxation. On the left panel partial melt is shown with red shading. (For interpretation of the references to color in this figure legend, the reader is referred to the web version of this article.)

found in the matrix surrounding the garnet. Ten different monazite grains returned identical $^{207}Pb/^{206}Pb$ dates that are more than 95% concordant with one exception (92%). The average $^{206}Pb/^{207}Pb$ age is 3443.4 ± 4.5 Ma, MSWD 1.09 (Fig. 6d), which does not change if the discordant data point is excluded.

5.3. Thermo-mechanical modeling

As the 15 km thick pile of continental flood basalt accumulates over a period of 140 Myr, the continental geotherm warms up to a point where partial melting affects a larger part of the buried crust (Fig. 7, West and Mareschal, 1979; Rey et al., 2003). The weakening of the partially molten crust facilitated partial convective overturn, which starts at about $t_0 + 141$ Myr with the rise of hot and light granitic domes and the coupled sinking of the denser greenstone pile. From $t_0 + 145$ Myr, several instabilities evolve; their length-scales (*ca.* 100 km in diameter) are compatible with granitoid domes of the EPGGT and other Archean cratons. Large segments of greenstones are buried and metamorphosed at lower crustal conditions. Sheared and stretched, these supracrustal rocks are exhumed as enclaves inside the domes. The model predicts that domes are prime locations for the sampling of supracrustal rocks that looped through the lower crust before their exhumation in the core of the domes.

The sagduction history and P–T paths recorded by particles initially located at different depths (10, 12.5, 20, 25, 30 and 40 km) is shown in Figs. 8a and 8b, respectively. During sagduction, these particles record a large range of apparent geothermal gradients between 10 and 45 °C/km. Our modeling suggests a maximum pressure of 14 kbar and a maximum temperature of 800 °C. In the first million year, after the onset of partial melting in the lower crust, the P–T–t path of the partially molted crust is complex due to transient convective motion. For simplification, we selected figures within the time window 1 to 30 Myr. Particles that lay on the interface between greenstone and protocrust (*ca.* 15 km depth, Fig. 9) show an increase of pressure related to the burial into the lower crust, followed by an increase of temperature and finally a decrease of pressure linked to exhumation in domes core. For some particles, the entire burial and exhumation history occurred within less than 5 Myr (Figs. 9a and 9b, blue and purple tracers). In addition, particles show different temperature-time and pressure-time evolutions (Fig. S5a and b). Temperature and pressure peaks are obtained over a 30 Myr period. Maximum of pressures are around 12–14 kbar compatible with a 45 km thick crust and reach amphibolite- to granulite-facies conditions ($T = 600$–800 °C). After exhumation, cooling of granitic domes occurred progressively over several tens of Myr (Fig. 7, right column). The comparison between Ellipsis P–T paths versus thermobarometric data highlights a robust agreement between the observed and modeled P–T ranges (Fig. 10). Different parageneses recorded by our sample (colored boxes) are in agreement with Ellipsis P–T–t path.

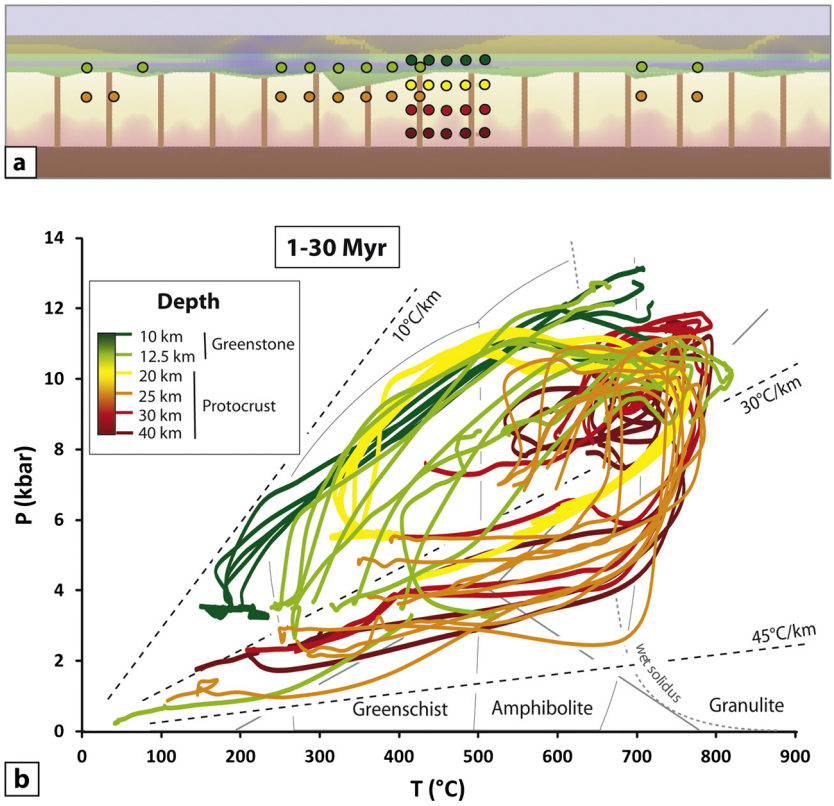

Fig. 8. Initial location of P–T tracers and corresponding P–T path between 1 and 30 Myr.

6. Discussion and implication for Archean sagduction

6.1. Crustal loop: an entire cycle of burial and exhumation

The thermobarometric data (Fig. 4) show a progressive increase of temperature from the margin (500 °C) to the core of the dome (represented by the enclave, 700 to 750 °C). As shown by Mareschal and West (1980), significant horizontal and vertical temperature gradients in the newly formed greenstone–granitoid association are able to produce lateral variations in metamorphic conditions, which are coherent with the large range of P–T conditions recorded for the Warrawoona greenstone belt (Figs. 4 and S3b) (see also Teyssier et al., 1990; Delor et al., 1991; Collins et al., 1998).

The felsic enclave equilibrated under amphibolite to granulite-facies conditions (650–750 °C and 4–7 kbar, Fig. S3a). In the different samples investigated (PB-11-23 and PB-11-28), sillimanite, biotite, plagioclase, K-feldspar occur both in the matrix and as inclusions in zircons. The occurrence of mineral inclusions of metamorphic origin indicates that the zircons, despite displaying weak oscillatory zoning, are likely of metamorphic origin (Fig. 5a). The low Th/U ratios (<0.088, Table 2) of most of the zircons analyzed in samples PB-11-23 and PB-11-28 further support a metamorphic origin (e.g. Williams and Claesson, 1987; Vavra et al., 1999; Rubatto, 2002; Bingen et al., 2004; Zheng et al., 2005). Additional evidence of zircon formation during metamorphism is provided by the oxygen isotopes. Exchange rates for oxygen in zircon are very slow (Watson and Cherniak, 1997) and can allow preservation of the protolith oxygen isotope composition during high-grade metamorphism (Valley et al., 1994). The zircon average ∂^{18}O values of Archean sedimentary rocks varies between 8.0 and 13.3‰ (Longstaffe and Schwarcz, 1977). Thus, the heavy ∂^{18}O isotopic composition (*ca.* 13‰, Fig. S4) of zircons in sample PB-11-23 and PB-11-28 (cores) is in line with a sedimentary origin for the enclave. The 3.3 Ga old zircon domains in both samples have the same ∂^{18}O values than the garnet core in metapelite PB-11-23 (*ca.* 12–13‰, Fig. S4). At temperatures of 650–750 °C, zircon and garnet do not significantly fractionate oxygen (Valley et al., 1994) and therefore if they formed in the same host rock, they should have the same oxygen isotope composition. Taken together, the felsic composition, the granulitic assemblage and the heavy oxygen isotope composition imply that the sedimentary rocks were buried down to the lower crust and exhumed back to the surface as large (tens of meters) enclaves within the dome. The deposition of the Charteris Formation is constrained at *ca.* 3315 Ma (Hickman, 1984) and the formation of zircon during high temperature metamorphism is dated at 3311.9 ± 4.9 Ma (PB-11-23, Fig. 6a) and 3314.6±3.3 Ma (cores in PB-11-28, Fig. 6b). These time constraints imply that the metasediment experienced burial and exhumation within a few million years.

This new dataset (petrological, thermobarometric, geochronological and geochemical) is consistent with our numerical simulations of sagduction. Our experiments confirm the P–T range (Fig. 10), the occurrence of supracrustal rocks buried and exhumed in the core of the domes (Fig. 9a) and indicate that the P–T–t evolution inherent to the formation of a keel and dome structure can accommodate such a rapid (i.e. <5 Myr) scenario of burial and exhumation (Fig. 9b).

The zircon rims in sample PB-11-28 show discordant dates (^{207}Pb/^{206}Pb from 1744 ± 5 Ma to 3264 ± 2 Ma, Fig. 6c) and point to a lower intercept of *ca.* 850 Ma. These zircon rims show a significantly lighter oxygen composition, with ∂^{18}O values between 4.3 and 8.7‰ (Fig. S4). Because of the small size of the zircon rims, it is possible that some of the age scattering reflect mixing ages. Alternatively, the scatter in ∂^{18}O values and U–Pb ages in the zircon rims could reflect different degrees of recrystallization. In any case, the formation for these zircon rims does not appear to be in equilibrium with the garnet core or rim. The low Mn-content of the garnet rim and an oxygen isotope composition (11.7‰, Table ST2) similar to that of the cores suggest some degree of garnet resorption during retrogression or melting, but still

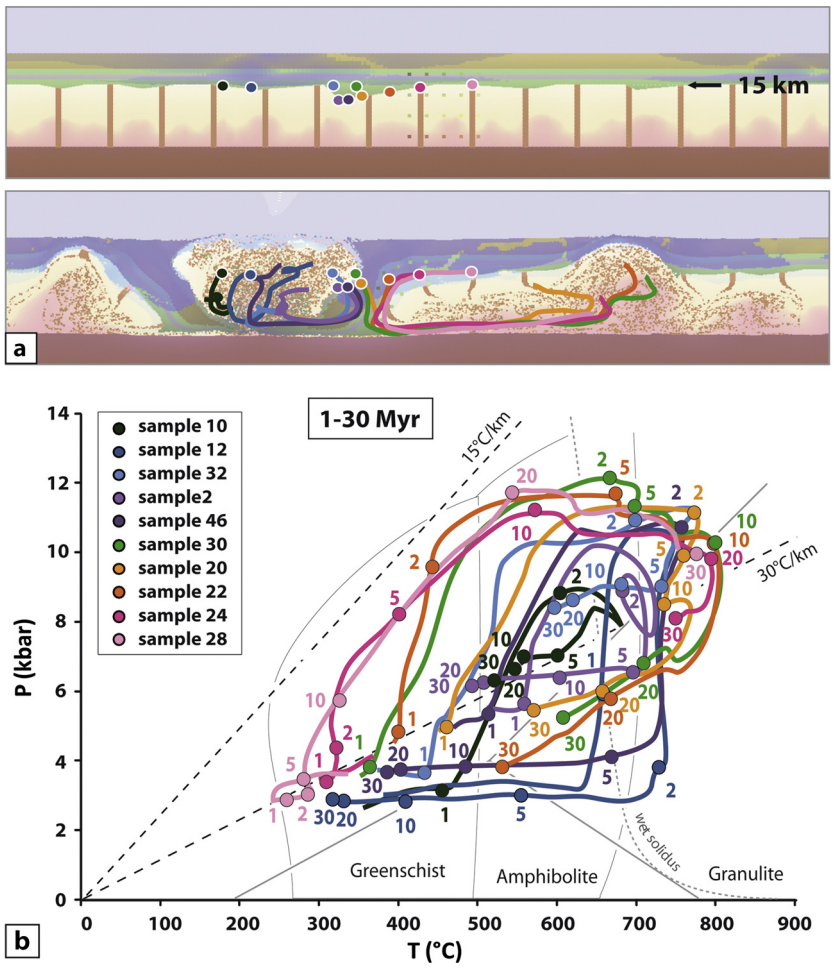

Fig. 9. (a) Tracers flow path for tracers initially located at the greenstone–protocrust boundary. (b) Corresponding P–T–t paths between 1 and 30 Myr. (For interpretation of the references to color in this figure, the reader is referred to the web version of this article.)

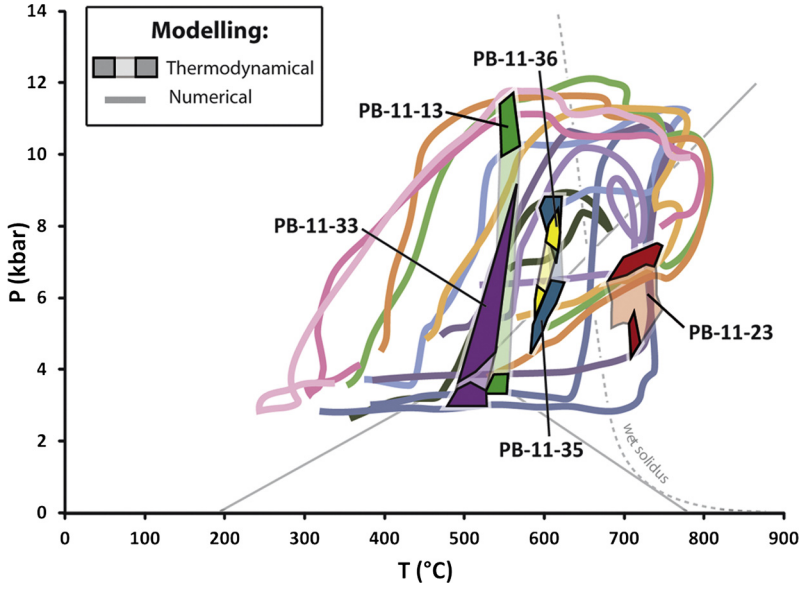

Fig. 10. Comparison between modeled P–T–t paths (Ellipsis) for particles initially located at the greenstone-protocrust interface and P–T paths extracted to our thermo-barometric study (Perple_X).

within the same bulk oxygen isotope composition as the zircon and garnet cores (respectively 13.1‰ and 12.7‰, Fig. S4). We suggest that the low $\partial^{18}O$ values of the zircon rims may reflect a later metamorphic reequilibration in a relatively ^{18}O-depleted environment, which is not preserved or was not recorded in the garnet.

6.2. A possible old metamorphic history

Monazites crystals included in garnet in sample PB-11-13 (Fig. 5b) contain mineral inclusions of biotite, plagioclase, quartz and apatite. Biotite is absent from the rock matrix but occurs in part as inclusions in the host garnet (which contains also staurolite, quartz, muscovite, apatite, ilmenite and rutile). The occurrence of the same minerals in monazites and in garnet on the one side, and in garnet and in the matrix on the other side, highlights two distinct parageneses.

The age of the monazite included in garnet (3443.4 ± 4.5 Ma, MSWD 1.09) is interpreted as dating an earlier metamorphic event. Considering the relatively high closure temperature of the U–Pb system for monazite (≥900 °C, Cherniak et al., 2004) and the thermal shielding potential of garnet for the U–Th–Pb system (DeWolf et al., 1993; Montel et al., 1996; Foster et al., 2000; Montel et al., 2000), we suggest that monazite included in garnet dates an earlier metamorphic event at 3443.4 ± 4.5 Ma and was not re-equilibrated during following metamorphic episodes that affected the rock matrix. This early metamorphism was coeval with the emplacement of the Warrawoona Group (*ca*. 3.53 to 3.43 Ga), which represents voluminous magmatism erupted onto a basement of older continental crust (Van Kranendonk et al., 2007). Crustal thickening due to magma emplacement may have caused partial melting at the base of the crust leading to the formation of the Callina and Tambina TTG Supersuites. We speculate that the monazite formed when the rock was initially buried at the base of Warrawoona Group in the lower to middle crust and was then overgrown by garnet during progressive metamorphism.

6.3. Implications for East Pilbara and Archean geodynamics

Archean processes have been investigated using a variety of methods including field geology and structures (e.g. Bouhallier et al., 1993; Chardon et al., 1998; Collins et al., 1998; Bédard et al., 2003; Peschler et al., 2004; Van Kranendonk et al., 2004), petrology (e.g. Hamilton, 1998; Brown, 2006, 2007, 2008) or geochemistry (e.g. Drummond and Defant, 1990; Martin, 1999; Green et al., 2000; Martin and Moyen, 2002). Archean processes have also been explored via numerical experiments (e.g. Gerya et al., 2000; van Hunen et al., 2004; O'Neil et al., 2007; van Hunen and van den Berg, 2008; Sizova et al., 2010; Moyen and Van Hunen, 2012; Johnson et al., 2014).

Archean geodynamics at crustal levels is often framed in the context of vertical *vs* horizontal tectonics. The numerical modeling presented here highlights that this debate is obsolete (see also Thébaud and Rey, 2013). Downward and upward flows driven by sagduction cannot occur without an equivalent amount of horizontal flow in the lower crust and upper crust respectively. Or model shows that sagduction of greenstone covers is accommodated by a number of mechanism including horizontal shortening, folds that can be asymmetric, overturned to recumbent folds, and nappes.

We emphasize that there is no incompatibility between subduction and sagduction, and that both processes may have co-existed in the Archean. In the East Pilbara, scenarios involving fold interferences and metamorphic core complexes have been proposed to explain the metamorphic and structural features of the dome and basin pattern (Kloppenburg et al., 2001; Blewett, 2002). However, none of these processes can explain the fast crustal loop observed in the Mount Edgar granitic dome. Sagduction and subduction are better suited to achieve fast burial and exhumation. Apparent geothermal gradients are often used as a proxy for tectonic settings. For instance, Archean apparent geothermal gradients of *ca*. 15 °C/km or lower are assumed for subduction–accretion zones (e.g. Moyen et al., 2006). The large range of apparent geothermal gradients documented in our numerical experiment (i.e. 10 to 45 °C/km, Fig. 8) includes gradients compatible with subduction zones. Indeed, sagduction and subduction alike involve the rapid burial of near-surface cool rocks. Therefore, low apparent geothermal gradients are expected in both cases. This suggests that the apparent geothermal gradient is not a robust parameter to characterize subduction or any particular tectonic setting.

Both subduction channels (Ernst et al., 1997; Ernst, 2006; Agard et al., 2009; Guillot et al., 2009) and sagduction settings adequately account for fast burial-exhumation loops, and both accounts for low-temperature gradients. The differences between sagduction and subduction may lie elsewhere. Sagduction is characterized by a regional dome and basin strain pattern particularly well preserved in the Pilbara because free of any major interference from plate boundary processes. However, when plate boundary forces interfere with the gravitational forces driving sagduction, the overall strain pattern becomes more ambiguous. In contrast to subduction, sagduction is a mechanically short-lived process, involving burst of rapid burial and exhumation coeval with peak of magmatic activities, followed by protracted slow thermal relaxation periods. This seems to be the case in the East Pilbara where a burst of magmatic activity at 3325 and 3290 Ma (Emu Pool Supersuite) is coeval with the fast burial and exhumation of crustal rocks, then followed by a long period of tectonic quiescence.

7. Conclusions

Petrology, thermobarometry, geochronology, geochemistry and numerical modeling of the rocks of the Mount Edgar Dome and Warrawoona Greenstone Belt we revealed important constraints on Archean tectonic. The P–T evolution of rock units over time defines a fast burial and exhumation cycle with burial of sedimentary sequences to lower crustal conditions and exhumation in dome by convection within a few Myr at around 3.31 Ga. We also identified a probable poly-metamorphic record in the metasediments of the Mount Edgar Dome starting from 3.44 Ga. The P–T–t path of these units is consistent with sagduction tectonic and adds significant details to the formation and the evolution of the Warrawoona granitoid-greenstone belt. Sagduction initiates as a response to density inversion and thermal weakening due to the emplacement of a thick volcanic rock pile onto a strongly radiogenic protocrust. Burial and exhumation of cold and dense greenstones is linked in time with crustal melting and granitoid dome formation.

The wide range of gradients obtained by modeling sagduction (i.e. 10–45 °C/km) does not support the conventional distinction between Archean intraplate sagduction having high apparent geothermal gradient (i.e. >25 °C/km) and plate boundaries tectonics, such as subduction, producing relatively low gradients (12–15 °C/km). Moreover, we observe that mid-pressure and high-temperature mineralogical assemblages that are commonly interpreted as collision can also be produced during sagduction. Similar petrological and thermobarometric characteristics can thus result from both sagduction and subduction/collision. Thereby, petrology and apparent geothermal gradients alone are not sufficient to discriminate between these two burial processes.

Acknowledgements

This paper has benefited from discussions with D. Marquer, C. Jaupart, C. Chopin, J. Hermann and many other colleagues from the Institut de Physique du Globe de Paris, the Sydney University and the Australian National University. Many thanks to P. Goncalves for inputs on thermobarometry study and Steve Mojzsis and Taras Gerya for constructive reviews of the paper. This work was supported by ANR eLife2 (ANR-10-BLAN-060) to P. Philippot, the financial support of the UnivEarthS Labex program at Sorbonne Paris Cité (ANR-10-LABX-0023 and ANR-11-IDEX-0005-02) and the

Australian Research Council's Discovery funding scheme (ARC DP 0342933) and AUSCOPE NCRIS and Computational Infrastructure for Geodynamics software infrastructure to P. Rey. This is IPGP contribution 3510.

Appendix A. Supplementary material

Supplementary material related to this article can be found online at http://dx.doi.org/10.1016/j.epsl.2014.04.025.

References

Abbott, D., Burgess, L., Longhi, J., Smith, W.H.F., 1994. An empirical thermal history of the Earth's upper mantle. J. Geophys. Res. 99 (B7), 13835–13850.

Abbott, D.H., Hoffman, S.E., 1984. Archaean plate tectonics revisited 1. Heat flow, spreading rate, and the age of subducting oceanic lithosphere and their effects on the origin and evolution of continents. Tectonics 3 (4), 429–448.

Agard, P., Yamato, P., Jolivet, L., Burov, E., 2009. Exhumation of oceanic blueschists and eclogites in subduction zones: timing and mechanisms. Earth-Sci. Rev. 92 (1), 53–79.

Anhaeusser, C.R., 1973. The evolution of the early Precambrian crust of southern Africa. Philos. Trans. R. Soc. Lond. Ser. A, Math. Phys. Sci. 273 (1235), 359–388.

Arndt, N.T., Nisbet, E.G., 1982. Komatiites. Taylor & Francis.

Barley, M.E., Pickard, A.L., 1999. An extensive, crustally-derived, 3325 to 3310 Ma silicic volcanoplutonic suite in the eastern Pilbara Craton: evidence from the Kelly Belt, McPhee Dome and Corunna Downs Batholith. Precambrian Res. 96 (1), 41–62.

Bédard, J.H., Brouillette, P., Madore, L., Berclaz, A., 2003. Archaean cratonization and deformation in the northern Superior Province, Canada: an evaluation of plate tectonic versus vertical tectonic models. Precambrian Res. 127 (1), 61–87.

Berman, R.G., 1988. Internally-consistent thermodynamic data for minerals in the system Na2O–K2O–CaO–MgO–FeO–Fe2O3–Al2O3–SiO2–TiO2–H2O–CO2. J. Petrol. 29 (2), 445–522.

Berman, R.G., 1990. Mixing properties of Ca–Mg–Fe–Mn garnets. Am. Mineral. 75, 328–344.

Bickle, M.J., 1986. Implications of melting for stabilisation of the lithosphere and heat loss in the Archaean. Earth Planet. Sci. Lett. 80 (3), 314–324.

Bickle, M.J., Bettenay, L.F., Boulter, C.A., Groves, D.I., Morant, P., 1980. Horizontal tectonic interaction of an Archean gneiss belt and greenstones, Pilbara block, Western Australia. Geology 8 (11), 525–529.

Bickle, M.J., Bettenay, L.F., Chapman, H.J., Groves, D.I., McNaughton, N.J., Campbell, I.H., De Laeter, J.R., 1993. Origin of the 3500–3300 Ma calc-alkaline rocks in the Pilbara Archaean: isotopic and geochemical constraints from the Shaw Batholith. Precambrian Res. 60 (1), 117–149.

Bickle, M.J., Morant, P., Bettenay, L.F., Boulter, C.A., Blake, T.S., Groves, D.I., 1985. Archaean tectonics of the Shaw Batholith, Pilbara Block, Western Australia: structural and metamorphic tests of the batholith concept. In: Evolution of Archean Supracrustal Sequences. In: Geological Association of Canada, Special Paper, vol. 28, pp. 325–341.

Bingen, B., Austrheim, H.k., Whitehouse, M.J., Davis, W.J., 2004. Trace element signature and U/Pb geochronology of eclogite-facies zircon, Bergen Arcs, Caledonides of W Norway. Contrib. Mineral. Petrol. 147 (6), 671–683.

Black, L.P., Kamo, S.L., Allen, C.M., Aleinikoff, J.N., Davis, D.W., Korsch, R.J., Foudoulis, C., 2003. TEMORA 1: a new zircon standard for Phanerozoic U/Pb geochronology. Chem. Geol. 200 (1), 155–170.

Blewett, R.S., 2000. North Pilbara 'Virtual' structural field trip. Geosci. Aust. Rec. 2000/45. http://www.ga.gov.au/rural/projects/pilbara/.

Blewett, R.S., 2002. Archaean tectonic processes: a case for horizontal shortening in the North Pilbara Granite–Greenstone Terrane, Western Australia. Precambrian Res. 113 (1), 87–120.

Blewett, R.S., Shevchenko, S., Bell, B., 2004. The North Pole Dome: a non-diapiric dome in the Archaean Pilbara Craton, Western Australia. Precambrian Res. 133 (1), 105–120.

Bouhallier, H., Chardon, D., Choukroune, P., 1995. Strain patterns in Archaean dome-and-basin structures: the Dharwar craton (Karnataka, South India). Earth Planet. Sci. Lett. 135 (1), 57–75.

Bouhallier, H., Choukroune, P., Ballèvre, M., 1993. Diapirism, bulk homogeneous shortening and transcurrent shearing in the Archaean Dharwar craton: the Holenarsipur area, southern India. Precambrian Res. 63 (1), 43–58.

Boulter, C.A., Bickle, M.J., Gibson, B., Wright, R.K., 1987. Horizontal tectonics predating upper Gorge Creek group sedimentation Pilbara block, Western Australia. Precambrian Res. 36 (3), 241–258.

Brace, W.F., Kohlstedt, D.L., 1980. Limits on lithospheric stress imposed by laboratory experiments. J. Geophys. Res., Solid Earth 85 (B11), 6248–6252.

Brown, M., 2006. Duality of thermal regimes is the distinctive characteristic of plate tectonics since the Neoarchean. Geology 34 (11), 961–964.

Brown, M., 2007. Metamorphism, plate tectonics, and the supercontinent cycle. Earth Sci. Front. 14 (1), 1–18.

Brown, M., 2008. Characteristic thermal regimes of plate tectonics and their metamorphic imprint throughout Earth history: when did Earth first adopt a plate tectonics mode of behavior? Spec. Pap., Geol. Soc. Am. 440, 97.

Buick, R., Des Marais, D.J., Knoll, A.H., 1995. Stable isotopic compositions of carbonates from the Mesoproterozoic Bangemall Group, northwestern Australia. Chem. Geol. 123 (1), 153–171.

Bürgmann, R., Dresen, G., 2008. Rheology of the lower crust and upper mantle: evidence from rock mechanics, geodesy, and field observations. Annu. Rev. Earth Planet. Sci. 36, 531–567.

Cagnard, F., Durrieu, N., Gapais, D., Brun, J.P., Ehlers, C., 2006. Crustal thickening and lateral flow during compression of hot lithospheres, with particular reference to Precambrian times. Terra Nova 18 (1), 72–78.

Carignan, J., Hild, P., Mevelle, G., Morel, J., Yeghicheyan, D., 2001. Routine analyses of trace elements in geological samples using flow injection and low pressure on-line liquid chromatography coupled to ICP-MS: a study of geochemical reference materials BR, DR–N, UB–N, AN–G and GH. Geostand. Newsl. 25 (2–3), 187–198.

Chardon, D., Choukroune, P., Jayananda, M., 1996. Strain patterns, décollement and incipient sagducted greenstone terrains in the Archaean Dharwar craton (South India). J. Struct. Geol. 18 (8), 991–1004.

Chardon, D., Choukroune, P., Jayananda, M., 1998. Sinking of the Dharwar basin (South India): implications for Archaean tectonics. Precambrian Res. 91 (1), 15–39.

Chatterjee, N.D., Froese, E., 1975. A thermodynamic study of the pseudobinary join muscovite-paragonite in the system KAlSi3O8–NaAlSi3O8–Al2O3–SiO2–H2O. Am. Mineral. 60, 985–993.

Cherniak, D.J., Watson, E.B., Grove, M., Harrison, T.M., 2004. Pb diffusion in monazite: a combined RBS/SIMS study. Geochim. Cosmochim. Acta 68 (4), 829–840.

Clemens, J.D., Petford, N., 1999. Granitic melt viscosity and silicic magma dynamics in contrasting tectonic settings. J. Geol. Soc. 156 (6), 1057–1060.

Collins, W.J., 1989. Polydiapirism of the Archean Mount Edgar Batholith, Pilbara Block, Western Australia. Precambrian Res. 43 (1), 41–62.

Collins, W.J., 1993. Melting of Archaean sialic crust under high aH2O conditions: genesis of 3300 Ma Na-rich granitoids in the Mount Edgar Batholith, Pilbara Block, Western Australia. Precambrian Res. 60 (1), 151–174.

Collins, W.J., Van Kranendonk, M.J., 1999. Model for the development of kyanite during partial convective overturn of Archean granite–greenstone terranes: the Pilbara Craton, Australia. J. Metamorph. Geol. 17 (2), 145–156.

Collins, W.J., Van Kranendonk, M.J., Teyssier, C., 1998. Partial convective overturn of Archaean crust in the east Pilbara Craton, Western Australia: driving mechanisms and tectonic implications. J. Struct. Geol. 20 (9), 1405–1424.

Coltice, N., Bertrand, H., Rey, P., Jourdan, F., Phillips, B.R., Ricard, Y., 2009. Global warming of the mantle beneath continents back to the Archaean. Gondwana Res. 15 (3), 254–266.

Condie, K.C., Benn, K., 2006. Archean geodynamics: similar to or different from modern geodynamics? In: Geophysical Monograph Series, vol. 164, pp. 47–59.

Connolly, J.A.D., 1990. Multivariable phase diagrams; an algorithm based on generalized thermodynamics. Am. J. Sci. 290 (6), 666–718.

Dallmeyer, R.D., 1978. $^{40}Ar/^{39}Ar$ incremental-release ages of hornblende and biotite across the Georgia Inner Piedmont, their bearing on late Paleozoic–early Mesozoic tectonothermal history. Am. J. Sci. 278 (2), 124–149.

de Bremond d'Ars, J., Lécuyer, C., Reynard, B., 1999. Hydrothermalism and diapirism in the Archean: gravitational instability constraints. Tectonophysics 304 (1), 29–39.

Delor, C., Burg, J.P., Clarke, G., 1991. C. R. Acad. Sci., Sér. 2 Méc. Phys. Chim. Sci. Univers Sci. Terre. Comptes rendus de l'Académie des sciences. Série 2, Mécanique, Physique, Chimie, Sciences de l'univers, Sciences de la Terre 312 (3), 257–263.

DeWolf, C.P., Belshaw, N., O'Nions, R.K., 1993. A metamorphic history from micron-scale $^{207}Pb/^{206}Pb$ chronometry of Archean monazite. Earth Planet. Sci. Lett. 120 (3), 207–220.

Dixon, J.M., Summers, J.M., 1983. Patterns of total and incremental strain in subsiding troughs: experimental centrifuged. models of inter-diapir synclines. Can. J. Earth Sci. 20 (12), 1843–1861.

Drummond, M.S., Defant, M.J., 1990. A model for trondhjemite–tonalite–dacite genesis and crustal growth via slab melting: Archean to modern comparisons. J. Geophys. Res., Solid Earth 95 (B13), 21503–21521.

Dymkova, D., Gerya, T., 2013. Porous fluid flow enables oceanic subduction initiation on Earth. Geophys. Res. Lett. 40 (21), 5671–5676.

Ernst, W.G., 2006. Preservation/exhumation of ultrahigh-pressure subduction complexes. Lithos 92 (3), 321–335.

Ernst, W.G., Maruyama, S., Wallis, S., 1997. Buoyancy-driven, rapid exhumation of ultrahigh-pressure metamorphosed continental crust. Proc. Natl. Acad. Sci. USA 94 (18), 9532–9537.

Flament, N., Rey, P.F., Coltice, N., Dromart, G., Olivier, N., 2011. Lower crustal flow kept Archean continental flood basalts at sea level. Geology 39 (12), 1159–1162.

Foster, G., Kinny, P., Vance, D., Prince, C., Harris, N., 2000. The significance of monazite U–Th–Pb age data in metamorphic assemblages; a combined study of monazite and garnet chronometry. Earth Planet. Sci. Lett. 181 (3), 327–340.

Fuhrman, M.L., Lindsley, D.H., 1988. Ternary-feldspar modeling and thermometry. Am. Mineral. 73 (3–4), 201–215.

Gerya, T.V., Perchuk, L.L., van Reenen, D.D., Smit, C.A., 2000. Two-dimensional numerical modeling of pressure–temperature–time paths for the exhumation of some granulite facies terrains in the Precambrian. J. Geodyn. 30 (1), 17–35.
Green, M.G., Sylvester, P.J., Buick, R., 2000. Growth and recycling of early Archaean continental crust: geochemical evidence from the Coonterunah and Warrawoona Groups, Pilbara Craton, Australia. Tectonophysics 322 (1), 69–88.
Guillot, S.p., Hattori, K., Agard, P., Schwartz, S.p., Vidal, O., 2009. Exhumation processes in oceanic and continental subduction contexts: a review. In: Subduction Zone Geodynamics. Springer, pp. 175–205.
Hamilton, W.B., 1998. Archean magmatism and deformation were not products of plate tectonics. Precambrian Res. 91 (1), 143–179.
Harris, L.B., Yakymchuk, C., Godin, L., 2012. Implications of centrifuge simulations of channel flow for opening out or destruction of folds. Tectonophysics 526, 67–87.
Harrison, T.M., 1982. Diffusion of ^{40}Ar in hornblende. Contrib. Mineral. Petrol. 78 (3), 324–331.
Harrison, T.M., Célérier, J., Aikman, A.B., Hermann, J., Heizler, M.T., 2009. Diffusion of 40Ar in muscovite. Geochim. Cosmochim. Acta 73 (4), 1039–1051.
Hickman, A.H., 1983. Geology of the Pilbara Block and Its Environs. Geological Survey of Western Australia Perth, Western Australia.
Hickman, A.H., 1984. Archaean diapirism in the Pilbara Block, Western Australia. In: Precambrian Tectonics Illustrated, pp. 113–127.
Hickman, A.H. Van Kranendonk, M.J., 2008. Marble Bar, WA Sheet 2855 1:100000, Western Australia Geological Survey.
Hoffman, P.F., 1988. United Plates of America, the birth of a craton-Early Proterozoic assembly and growth of Laurentia. Annu. Rev. Earth Planet. Sci. 16, 543–603.
Hoffman, P.F., Ranalli, G., 1988. Archean oceanic flake tectonics. Geophys. Res. Lett. 15 (10), 1077–1080.
Holland, T.J.B., Powell, R., 1998. An internally consistent thermodynamic data set for phases of petrological interest. J. Metamorph. Geol. 16 (3), 309–343.
Ickert, R.B., Hiess, J., Williams, I.S., Holden, P., Ireland, T.R., Lanc, P., Schram, N., Foster, J.J., Clement, S.W., 2008. Determining high precision, in situ, oxygen isotope ratios with a SHRIMP II: analyses of MPI-DING silicate-glass reference materials and zircon from contrasting granites. Chem. Geol. 257 (1), 114–128.
Jaupart, C., Labrosse, S., Mareschal, J.C., 2007. Temperatures, heat and energy in the mantle of the Earth. In: Treatise on Geophysics, vol. 7, pp. 253–303.
Johnson, T.E., Brown, M., Kaus, B.J.P., VanTongeren, J.A., 2014. Delamination and recycling of Archaean crust caused by gravitational instabilities. Nat. Geosci. 7.
Karato, S.-i., Wu, P., 1993. Rheology of the upper mantle: a synthesis. Science 260 (5109), 771–778.
Keller, T., May, D.A., Kaus, B.J.P., 2013. Numerical modelling of magma dynamics coupled to tectonic deformation of lithosphere and crust. Geophys. J. Int. 195 (3), 1406–1442.
Kloppenburg, A., 2003. Structural evolution of the Marble Bar Domain, Pilbara granite–greenstone terrain, Australia: the role of Archaean mid-crustal detachments. Rijksuniversiteit Utrecht, Inst. voor Aardwetenschappen.
Kloppenburg, A., White, S.H., Zegers, T.E., 2001. Structural evolution of the Warrawoona Greenstone Belt and adjoining granitoid complexes, Pilbara Craton, Australia: implications for Archaean tectonic processes. Precambrian Res. 112 (1), 107–147.
Kretz, R., 1983. Symbols for rock-forming minerals. Am. Mineral. 68, 277–279.
Le Hebel, F., Rey, P., 2005. Metamorphism–deformation relationships in a mid-archean granite-greenstones terrane: deciphering between metamorphic core complex and diapiric models. The example of The East Pilbara craton (Western Australia). Geophys. Res. Abstr. 7, 06113.
Le Hebel, F., Rey, P., Thebaud, N., Van Kranendonk, M., 2005. Deformation Mechanism, Rheology and Tectonics 2005. Deformation Mechanism, Rheology and Tectonics.
Longstaffe, F.J., Schwarcz, H.P., 1977. sol18O16O of Archean clastic metasedimentary rocks: a petrogenetic indicator for Archean gneisses? Geochim. Cosmochim. Acta 41 (9), 1303–1312.
Ludwig, K.R., 2001. Isoplot/Ex version 2.49. A geochronological toolkit for Microsoft Excel. Berkeley Geochronology Center. Special Publication No. 1a, 55 pp.
Macgregor, A.M., 1951. Some milestones in the Precambrian of Southern Rhodesia. Proc. Geol. Soc. S. Afr. 54, 27–71.
Mäder, U.K., Percival, J.A., Berman, R.G., 1994. Thermobarometry of garnet–clinopyroxene–hornblende granulites from the Kapuskasing structural zone. Can. J. Earth Sci. 31 (7), 1134–1145.
Mareschal, J.-C., West, G.F., 1980. A model for Archean tectonism. Part 2. Numerical models of vertical tectonism in greenstone belts. Can. J. Earth Sci. 17 (1), 60–71.
Martin, H., 1999. Adakitic magmas: modern analogues of Archaean granitoids. Lithos 46 (3), 411–429.
Martin, H., Moyen, J.-F., 2002. Secular changes in tonalite–trondhjemite–granodiorite composition as markers of the progressive cooling of Earth. Geology 30 (4), 319–322.
Martin, L.A., Rubatto, D., Crépisson, C., Hermann, J., Putlitz, B., Vitale-Brovarone, A., 2014. Garnet oxygen analysis by SHRIMP-SI: matrix corrections and application to high pressure metasomatic rocks from Alpine Corsica. Chem. Geol 374, 25–36.
McMullin, D.W.A., Berman, R.G., Greenwood, H.J., 1991. Calibration of the SGAM thermobarometer for pelitic rocks using data from phase-equilibrium experiments and natural assemblages. Can. Mineral. 29 (4), 889–908.
McNaughton, N.J., Compston, W., Barley, M.E., 1993. Constraints on the age of the Warrawoona Group, eastern Pilbara block, Western Australia. Precambrian Res. 60 (1), 69–98.
Montel, J.-M., Foret, S., Veschambre, M.l., Nicollet, C., Provost, A., 1996. Electron microprobe dating of monazite. Chem. Geol. 131 (1), 37–53.
Montel, J.M., Kornprobst, J., Vielzeuf, D., 2000. Preservation of old U–Th–Pb ages in shielded monazite: example from the Beni Bousera Hercynian kinzigites (Morocco). J. Metamorph. Geol. 18 (3), 335–342.
Moresi, L., Dufour, F.d.r., Mühlhaus, H.B., 2002. Mantle convection modeling with viscoelastic/brittle lithosphere: numerical methodology and plate tectonic modeling. Pure Appl. Geophys. 159 (10), 2335–2356.
Moresi, L., Muhlhaus, H.B., Dufour, F., 2001. Particle-in-cell solutions for creeping viscous flows with internal interfaces. In: Bifurcation and Localization in Soils and Rocks, pp. 345–353.
Moyen, J.-F., Stevens, G., Kisters, A., 2006. Record of mid-Archaean subduction from metamorphism in the Barberton terrain, South Africa. Nature 442 (7102), 559–562.
Moyen, J.-F., Van Hunen, J., 2012. Short-term episodicity of Archaean plate tectonics. Geol. Soc. (Lond.) Spec. Publ. 40 (5), 451–454.
Nelson, D.R., 1997. Evolution of the Archaean granite–greenstone terranes of the Eastern Goldfields, Western Australia: SHRIMP U/Pb zircon constraints. Precambrian Res. 83 (1), 57–81.
Nelson, D.R., 1998. Granite–greenstone crust formation on the Archaean Earth: a consequence of two superimposed processes. Earth Planet. Sci. Lett. 158 (3), 109–119.
Nelson, D.R., 1999. Compilation of Geochronology Data, 1998. Geol. Surv. West. Aust., ISBN 0730966445.
Nelson, D.R., 2001a. Compilation of Geochronology Data, 2000. Geol. Surv. West. Aust., ISBN 0730756947.
Nelson, D.R., 2001b. An assessment of the determination of depositional ages for Precambrian clastic sedimentary rocks by U/Pb dating of detrital zircons. Sediment. Geol. 141, 37–60.
O'Neil, J., Maurice, C., Stevenson, R.K., Larocque, J., Cloquet, C., David, J., Francis, D., 2007. The geology of the 3.8 Ga Nuvvuagittuq (Porpoise Cove) greenstone belt, northeastern superior province, Canada. Dev. Precambrian Geol. 15, 219–250.
Pawley, M.J., Van Kranendonk, M.J., Collins, W.J., 2004. Interplay between deformation and magmatism during doming of the Archaean Shaw granitoid complex, Pilbara craton, Western Australia. Precambrian Res. 131 (3), 213–230.
Percival, J.A., Stern, R.A., Skulski, T., Card, K.D., Mortensen, J.K., Begin, N.J., 1994. Minto block, superior province: missing link in deciphering assembly of the craton at 2.7 Ga. Geology 22 (9), 839–842.
Peschler, A.P., Benn, K., Roest, W.R., 2004. Insights on Archean continental geodynamics from gravity modelling of granite–greenstone terranes. J. Geodyn. 38 (2), 185–207.
Pidgeon, R.T., 1978. 3450-My-old volcanics in the Archaean layered greenstone succession of the Pilbara Block, Western Australia. Earth Planet. Sci. Lett. 37 (3), 421–428.
Ramberg, H., 1967. Model experimentation of the effect of gravity on tectonic processes. Geophys. J. R. Astron. Soc. 14 (1–4), 307–329.
Rey, P.F., Philippot, P., Thébaud, N., 2003. Contribution of mantle plumes, crustal thickening and greenstone blanketing to the 2.75–2.65 Ga global crisis. Precambrian Res. 127 (1), 43–60.
Robin, C.M.I., Bailey, R.C., 2009. Simultaneous generation of Archean crust and subcratonic roots by vertical tectonics. Geology 37 (6), 523–526.
Rubatto, D., 2002. Zircon trace element geochemistry: partitioning with garnet and the link between U/Pb ages and metamorphism. Chem. Geol. 184 (1), 123–138.
Sizova, E., Gerya, T., Brown, M., Perchuk, L.L., 2010. Subduction styles in the Precambrian: insight from numerical experiments. Lithos 116 (3), 209–229.
Smithies, R.H., 2000. The Archaean tonalite–trondhjemite–granodiorite (TTG) series is not an analogue of Cenozoic adakite. Earth Planet. Sci. Lett. 182 (1), 115–125.
Smithies, R.H., Champion, D.C., Cassidy, K.F., 2003. Formation of Earth's early Archaean continental crust. Precambrian Res. 127 (1), 89–101.
Smithies, R.H., Van Kranendonk, M.J., Champion, D.C., 2007. The Mesoarchean emergence of modern-style subduction. Gondwana Res. 11 (1), 50–68.
Stern, R.A., Bodorkos, S., Kamo, S.L., Hickman, A.H., Corfu, F., 2009. Measurement of SIMS instrumental mass fractionation of Pb isotopes during zircon dating. Geostand. Geoanal. Res. 33 (2), 145–168.
Taylor, S.R., McLennan, S.M., 1985. The Continental Crust: Its Composition and Evolution. Blackwell Scientific Publication, Carlton, 312 pp. OSTI ID: 6582885.
Taylor, S.R., McLennan, S.M., 1986. The chemical composition of the Archaean crust. Geol. Soc. (Lond.) Spec. Publ. 24 (1), 173–178.
Teyssier, C., Collins, W.J., Van Kranendonk, M.J., 1990. Strain and kinematics during the emplacement of the Mount Edgar Batholith and Warrawoona Syncline, Pilbara Block, Western Australia. In: Geoconferences (WA). Perth, Western Australia, pp. 481–483.
Thébaud, N., Philippot, P., Rey, P., Brugger, J.l., Van Kranendonk M, M., Grassineau, N., 2008. Protracted fluid–rock interaction in the Mesoarchaean and implication for gold mineralization: example from the Warrawoona syncline (Pilbara, Western Australia). Earth Planet. Sci. Lett. 272 (3), 639–655.

Thébaud, N., Philippot, P., Rey, P., Cauzid, J., 2006. Composition and origin of fluids associated with lode gold deposits in a Mesoarchean greenstone belt (Warrawoona Syncline, Pilbara Craton, Western Australia) using synchrotron radiation X-ray fluorescence. Contrib. Mineral. Petrol. 152 (4), 485–503.

Thébaud, N., Rey, P.F., 2013. Archean gravity-driven tectonics on hot and flooded continents: controls on long-lived mineralised hydrothermal systems away from continental margins. Precambrian Res. 229, 93–104.

Thorpe, R.I., Hickman, A., Davis, D.W., Mortensen, J.K., Trendall, A.F., 1992. U/Pb zircon geochronology of Archaean felsic units in the Marble Bar region, Pilbara Craton, Western Australia. Precambrian Res. 56 (3), 169–189.

Valley, J.W., Chiarenzelli, J.R., McLelland, J.M., 1994. Oxygen isotope geochemistry of zircon. Earth Planet. Sci. Lett. 126 (4), 187–206.

Van Haaften, W.M., White, S.H., 1998. Evidence for multiphase deformation in the Archean basal Warrawoona Group in the Marble Bar area, east Pilbara, Western Australia. Precambrian Res. 88 (1), 53–66.

Van Haaften, W.M., White, S.H., 2001. Reply to comment on "Evidence for multiphase deformation in the Archaean basal Warrawoona group in the Marble Bar area, East Pilbara, Western Australia (van Haaften, W.M., White, S.H., 1998. Precambrian Research 88, 53–66) by MJ, Van Kranendonk, AH Hickman, WJ, Collins". Precambrian Res. 105 (1), 79–84.

van Hunen, J., van den Berg, A.P., 2008. Plate tectonics on the early Earth: limitations imposed by strength and buoyancy of subducted lithosphere. Lithos 103 (1), 217–235.

van Hunen, J., van den Berg, A.P., Vlaar, N.J., 2004. Various mechanisms to induce present-day shallow flat subduction and implications for the younger Earth: a numerical parameter study. Phys. Earth Planet. Inter. 146 (1), 179–194.

Van Kranendonk, M.J., Collins, W.J., Hickman, A., Pawley, M.J., 2004. Critical tests of vertical vs. horizontal tectonic models for the Archaean East Pilbara granite–greenstone terrane, Pilbara craton, Western Australia. Precambrian Res. 131 (3), 173–211.

Van Kranendonk, M.J., Hickman, A.H., Collins, W.J., 2001. Comment on "Evidence for multiphase deformation in the Archaean basal Warrawoona group in the Marble Bar area, East Pilbara, Western Australia. by van Haaften, WM, White, SH, 1998: Precambrian Research 88, 53–66". Precambrian Res. 105 (1), 73–78.

Van Kranendonk, M.J., Hickman, A.H., Smithies, R.H., Nelson, D.R., Pike, G., 2002. Geology and tectonic evolution of the Archean North Pilbara terrain, Pilbara Craton, Western Australia. Econ. Geol. 97 (4), 695–732.

Van Kranendonk, M.J., Hugh Smithies, R., Hickman, A.H., Champion, D.C., 2007. Review: secular tectonic evolution of Archean continental crust: interplay between horizontal and vertical processes in the formation of the Pilbara Craton, Australia. Terra Nova 19 (1), 1–38.

Vavra, G., Schmid, R., Gebauer, D., 1999. Internal morphology, habit and U–Th–Pb microanalysis of amphibolite-to-granulite facies zircons: geochronology of the Ivrea Zone (Southern Alps). Contrib. Mineral. Petrol. 134 (4), 380–404.

Watson, E.B., Cherniak, D.J., 1997. Oxygen diffusion in zircon. Earth Planet. Sci. Lett. 148 (3), 527–544.

Wellman, P., 2000. Upper crust of the Pilbara Craton, Australia, 3D geometry of a granite/greenstone terrain. Precambrian Res. 104 (3), 175–186.

West, G.F., Mareschal, J.C., 1979. A model for Archean tectonism. Part I. The thermal conditions. Can. J. Earth Sci. 16 (10), 1942–1950.

Williams, I.S., 1998. U–Th–Pb geochronology by ion microprobe. In: McKibben, M.A., Shanks III, W.C., Ridley, W.I. (Eds.), Application of Microanalytical Techniques to Understanding Mineralizing Processes. In: Reviews in Economic Geology, vol. 7. Society of Economic Geologists Littleton, Colorad, pp. 1–35.

Williams, I.R., Bagas, L., 2007. Geology of the Mount Edgar 1 : 100 000 Sheet. Geological Survey of Western Australia.

Williams, I.S., Claesson, S., 1987. Isotopic evidence for the Precambrian provenance and Caledonian metamorphism of high grade paragneisses from the Seve Nappes, Scandinavian Caledonides. Contrib. Mineral. Petrol. 97 (2), 205–217.

Williams, I.S., Collins, W.J., 1990. Granite–greenstone terranes in the Pilbara Block, Australia, as coeval volcano-plutonic complexes, evidence from U–Pb zircon dating of the Mount Edgar Batholith. Earth Planet. Sci. Lett. 97 (1), 41–53.

Zegers, T.E., White, S.H., De Keijzer, M., Dirks, P., 1996. Extensional structures during deposition of the 3460 Ma Warrawoona Group in the eastern Pilbara Craton, Western Australia. Precambrian Res. 80 (1), 89–105.

Zheng, Y.-F., Zhou, J.-B., Wu, Y.-B., Xie, Z., 2005. Low-grade metamorphic rocks in the Dabie-Sulu orogenic belt: a passive-margin accretionary wedge deformed during continent subduction. Int. Geol. Rev. 47 (8), 851–871.